

The Galactic Chemical Evolution of Carbon
Implications for Stellar Nucleosynthesis

Undergraduate Research Thesis

Presented in partial fulfillment of the requirements for graduation *with research distinction in Astronomy and Astrophysics* in the College of Arts and Sciences of
The Ohio State University

by

Daniel Alexander Boyea

The Ohio State University
April 2023

Project Advisors
Professor David H. Weinberg, Department of Astronomy
James W. Johnson, Department of Astronomy

Abstract

Stellar evolution models provide uncertain predictions for elemental yields due to uncertainties in stellar physics. Here, I constrain the nucleosynthetic yields of C using multizone Galactic chemical evolution models. By matching the slopes of the [C/Mg]-[Mg/H] and [C/Mg]-[Mg/Fe] relationships in a sample of APOGEE subgiant stars, I find that massive stars and low mass stars contribute $\sim 80\%$ and $\sim 20\%$ of total C production respectively. To also match the normalization of the trends, I estimate the massive star C/Mg yield ratio $y_C^{\text{CC}}/y_{\text{Mg}}^{\text{CC}} = 1.57 + 0.59 (Z/Z_\odot)$, which explains the [C/Mg]-[Mg/H] trend when including the low mass C contribution. Variations in the star formation history only slightly impact the low [Mg/Fe] tail of the [C/Mg]-[Mg/Fe] relation. However, most of the scatter in the [C/Mg]-[Mg/H] distribution can be attributed to measurement errors and radial migration. Due to the degeneracy between the normalization of elemental yields and the strength of mass-loading in Galactic outflows, I constrain only the *relative* yield of C and Mg from a simple stellar population and the metallicity dependence thereof. While measurements of gas-phase C abundances are challenging, my model is broadly consistent with the [C/O]-[O/H] trend observed in compiled literature measurements.

Acknowledgements

I know I am guilty of skimming the acknowledgements of many works, but I dearly hope that the people who helped me complete this project will appreciate how much they have helped me. This year has been an incredibly challenging journey—and perhaps I am not open enough about what it has been like. I genuinely would have not made it to this day without everyone's help, one way or another.

James Johnson—your mentorship and guidance throughout this project was critical. You helped me learn an incredible amount about being an astronomer, and I am forever grateful for how you have guided this project, through late nights and last minute comments. Wayne, for everything you do for everyone—you are the glue holding together our department and nobody can say thank you enough. David and Jennifer for helping this project move forward, by providing guidance at critical junctions and being part of my committee. Rolando, for being the non-astronomer thrown into this work, and pointing out the flaw of incomprehensibility in this work.

Even though you may have not been able to help me with the science, dear friends and family, you have been no less important in the completion of this work. Eric, even across the country, you have always been a point of support and stability, and I am always happy to be around you. Anya, you are a wonderful friend and I cannot thank you enough for your unconditional support this year. All my friends who are just wonderful, inspiring, and incredible people—Kaia, Maria, Autumn, Simon, Bailee, Aaliyah, Sanskruti, Alyssa, Harrison, Denis, Keith, and so many others. And my family (including Arya, my most lovable doodle)—I cannot even begin to thank you enough for simply helping me recover my health and make it to graduation.

Table of Contents

| | |
|---|-----------|
| Abstract | i |
| Acknowledgements | ii |
| List of Figures | v |
| List of Tables | vi |
| 1 Introduction | 1 |
| 2 Nucleosynthesis | 4 |
| 2.1 Asymptotic Giant Branch Stars | 5 |
| 2.2 Core Collapse Supernovae | 9 |
| 3 The Equilibrium Approximation | 12 |
| 3.1 Yield Models | 13 |
| 3.2 Uncertainties | 14 |
| 4 The Multizone Model | 17 |
| 5 Multizone Model Results | 19 |
| 5.1 Data Selection | 19 |
| 5.2 The Evolution of C Abundances in the Galaxy | 19 |
| 5.3 Alternate Models | 20 |
| 5.4 Star Formation History | 22 |
| 5.5 Outflows | 25 |
| 5.6 Scatter | 26 |
| 5.7 Gas-Phase C Abundances | 26 |
| 6 Conclusions | 30 |

| | |
|---|-----------|
| Bibliography | 32 |
| Appendix | 40 |
| A.1 The APOGEE Subgiant Sample | 40 |
| A.2 Additional Considerations of Yields | 43 |
| A.3 Software | 45 |
| Symbols | 46 |
| Stellar Yield Models | 47 |
| Acronyms | 48 |
| Glossary | 49 |

List of Figures

| | | |
|----|--|----|
| 1 | APOGEE Subgiants | 3 |
| 2 | The periodic table of elements. Taken from Johnson (2019). | 6 |
| 3 | Low mass C yields | 8 |
| 4 | C yields delay time distribution | 8 |
| 5 | Low mass yield metallicity dependence | 9 |
| 6 | Massive star C yields | 11 |
| 7 | Reverse fit yields | 15 |
| 8 | C chemical evolution tracks | 21 |
| 9 | Mean stellar abundance trends | 22 |
| 10 | Adjusted yield models | 23 |
| 11 | Lateburst models | 24 |
| 12 | Reduced-outflow models | 26 |
| 13 | Scatter agreement | 27 |
| 14 | C/N abundance agreement | 28 |
| 15 | Gas phase abundances | 29 |
| A1 | Subgiant selection | 41 |
| A2 | Alternate low mass star yield models | 44 |
| A3 | Magnesium yields | 44 |
| A4 | Adjusting type Ia iron | 45 |

List of Tables

| | | |
|---|--|----|
| 1 | Fiducial Model | 5 |
| 2 | Low mass star solar C yields | 24 |

1. Introduction

Galactic chemical evolution (GCE) aims to understand the chemical and star formation histories of galaxies. At the core of GCE models are stellar yields—the amount of each chemical element stars produce (or destroy). Each element is produced in different amounts by different stars, leaving traces of the Galaxy’s evolutionary history. Through *Galactic Archeology*, we can reconstruct the history of our galaxy by investigating clues left behind in stars.

Here, I aim to understand C enrichment—where it is produced and how its abundances evolve over time. C is unique nucleosynthetically, one of few light elements (along with N) produced in asymptotic giant branch (AGB) stars (e.g. Johnson 2019; Karakas & Lattanzio 2014). C and N are well-studied elements since they are easy to observe in stellar spectra, even at the lowest metallicities (e.g. Fabbian et al. 2009; Nissen et al. 2014; Lambert & Ries 1981; Laird 1985; Lambert et al. 1986). Additionally, C and N are used as age indicators in red giant branch stars (Martig et al. 2016; Masseron & Gilmore 2015; Hasselquist et al. 2019; Vincenzo et al. 2021).

Gas-phase [C/O] ratios¹—observed in very low metallicity, high redshift damped Lyman-alpha systems (DLA)—decrease with increasing [O/H] (Frebel & Norris 2015; Cooke et al. 2017). Then, [C/O] increases above [O/H] ≈ -1 (Berg et al. 2019; see discussion in section 5.7). While we know C is produced in AGB stars and core collapse supernovae (CCSNE), we still have a limited understanding of the magnitude and metallicity-dependence of each process.

Despite their central role in GCE models, nucleosynthetic yields predicted by stellar evolution models are rife with uncertainties. The production rates of elements in stars are shaped by poorly understood processes, including mass loss, opacity, nuclear reaction rates, rotational mixing, and convection (Karakas & Lattanzio 2014; Ventura et al. 2013; Limongi & Chieffi 2018). Changes in massive stars’ ex-

¹In this paper, I use the standard notation for chemical abundances. $[A/B] = \log_{10}(A/B) - \log_{10}(A_{\odot}/B_{\odot})$, i.e. $[A/B]$ is the logarithm of the ratio between A and B, scales such that $[A/B] = 0$ for the sun. Solar abundances are as measured in Asplund et al. (2009)

plodability also introduce further variation and uncertainty in population-averaged yields (Griffith et al. 2021).

GCE models typically use unmodified nucleosynthetic predictions and attempt to create models matching observations by varying the star formation history (SFH) and other evolutionary parameters. Here, I introduce C yields as an additional free parameter, determining which yield prescriptions reproduce Galactic abundance trends. Johnson et al. (2023) examined similar GCE models of N, an element whose production is closely related to C. Johnson et al. (2023) found that trends in N and O abundances can be explained by the metallicity dependence of relative N and O yields. Here, I extend their models to C and show that similar constraints on C and O relative yields can be obtained from observed abundance ratios. Additionally, I assess which yield prescriptions reproduce Galactic abundance trends while assessing the impact of GCE model assumptions, such as SFH and outflow mass loading.

Accurate determination of stellar birth abundances for C and N is challenging. When a star enters the red giant branch, material from the CNO-processed core is mixed with the envelope in first dredge up, enhancing N and depleting C (Iben 1967; Vincenzo et al. 2021; Karakas & Lattanzio 2014). Measurements of these evolved stars' atmospheres will no longer reflect their birth abundances. Additionally, gas-phase measurements of C are extremely limited as C lacks strong lines in HII regions (Skillman et al. 2020).

To this end, I use a sample of subgiant stars from the Apache Point Observatory Galactic Evolution Experiment (APOGEE) (Majewski et al. 2017). According to stellar evolution theory and observations (Gilroy 1989; Korn et al. 2007; Lind et al. 2008; Souto et al. 2018, 2019), these stars have not yet experienced first dredge up but have well-mixed photospheres. Their photospheric abundances should thus represent their birth composition. In Fig. 1, I plot this sample, selected by the criteria in Roberts et al. (2023, in prep; see Appendix A.1). These empirical results contain information on the relative C and Mg yields, which I use later in this work.

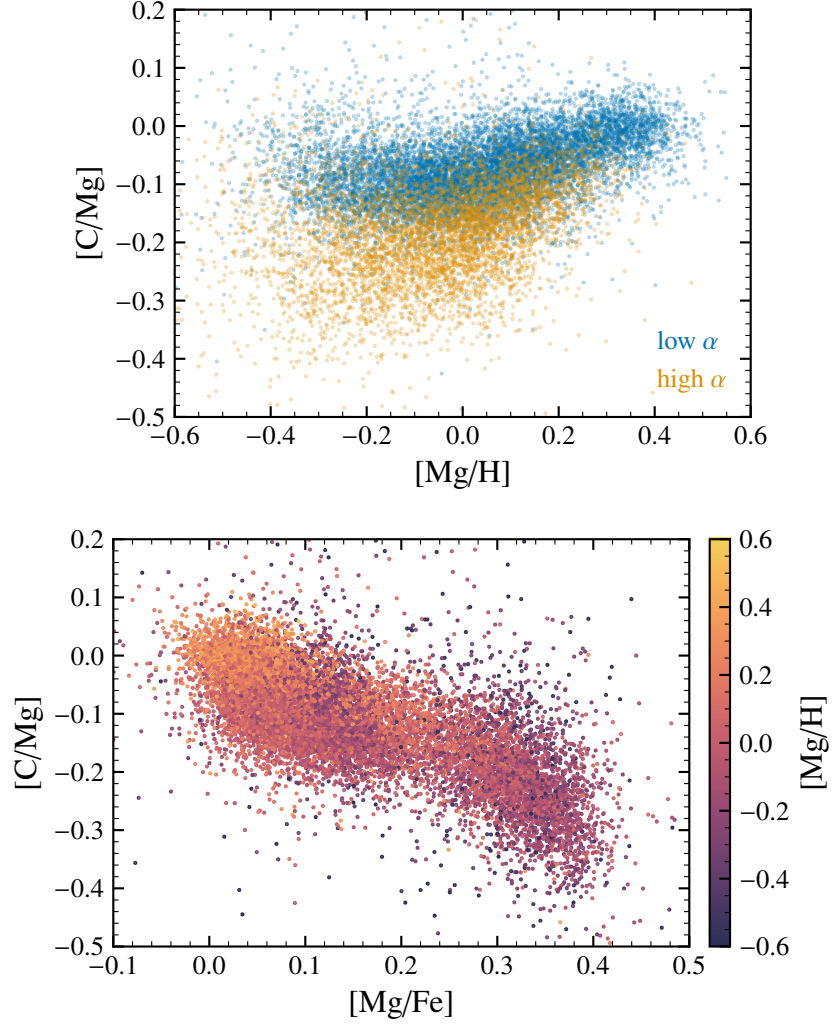


Figure 1: The $[C/Mg]$ ratio against $[Mg/H]$ (top) and $[Mg/Fe]$ (bottom) for the Roberts et al. (2023, in prep.) sample of APOGEE subgiants. On the top, I plot high and low- α stars in blue and orange, using the separation defined in Equation A2. On the bottom, I color-code stars according to their $[Mg/H]$ abundance.

2. Nucleosynthesis

Theoretical models of stellar nucleosynthesis provide the starting point of this investigation. I focus on three primary nucleosynthetic pathways: AGB stars, CCSNE, and supernovae type Ia (SNE Ia). Each process has unique timescales and yields, traceable through the tools of GCE. I compare C, produced in CCSNE and AGB stars, to Mg and Fe as tracers of CCSNE and SNE Ia respectively.

When a single stellar population (SSP) forms, CCSNE are the first enrichment event. CCSNE explode within $\lesssim 40$ Myr, providing light elements (C, O, and Mg) and heavier elements (Fe and beyond). Metallicity-independent yields from CCSNE are the only statistically significant source of O and Mg (α elements). Next, low-mass stars begin to reach the end of their lives. By shedding their outer layers, AGB stars are important sources of C, N, and neutron capture elements. Finally, white dwarfs explode, releasing Fe and other iron-peak elements.

For an element X and star with mass M , the stellar yield \tilde{y} is defined as the net production of X relative to M , or

$$\tilde{y}_X = \frac{M_{X, \text{ejected}} - Z_{0,X} M_{\text{ejected}}}{M} \quad (1)$$

where M_{ejected} and $M_{X, \text{ejected}}$ are the total ejected mass of the envelope and the element X, respectively. For example, if a $1 M_{\odot}$ star has $\tilde{y}_C = 10^{-3}$, then the star will add $10^{-3} M_{\odot}$ of C to the interstellar medium. Although per-star yields are necessary to compute AGB star enrichment rates in GCE models, IMF-averaged yields are useful in interpreting their predictions. For a yield y from a star of mass M and initial metallicity Z , the IMF-averaged yield is given by

$$y_X(Z) = \int_{M_{\min}}^{M_{\max}} \tilde{y}_X(M, Z) \frac{dN}{dM} dM \quad (2)$$

where dN/dM is the normalized initial mass function (IMF), and M_{\min} and M_{\max} are the minimum and maximum mass of stars, which I take to be $0.08 M_{\odot}$ and $100 M_{\odot}$ respectively. For AGB stars, the yields are truncated above $8 M_{\odot}$. To calculate the

Table 1: Yields for the fiducial model in units of SSP birth mass. See section 2.1 for the definition of C11.

| Element | y_{C}^{CC} | \tilde{y}^{AGB} | y^{SNeIa} |
|---------|-------------------------------|----------------------------------|--------------------|
| C | $0.0028 + 0.001(Z/Z_{\odot})$ | $2.9 \times \text{C11}$ | 0 |
| Mg | 0.00185 | 0 | 0 |
| Fe | 0.0012 | 0 | 0.00214 |
| N | 0.00072 | $9 \times 10^{-4}(Z/Z_{\odot})M$ | 0 |

IMF-weighted net yields, I use the Versatile Integrator for Chemical Evolution code (VICE¹).

To focus on C yields, I adapt the yield choices of other elements from Johnson et al. (2021, 2023). Table 1 contains my fiducial yields, in units of a SSP’s birth mass. Also following Johnson et al. (2021, 2023), I take the SNE Ia delay time distribution to be a $t^{-1.1}$ power-law suggested by the observations of Maoz et al. (2012).

2.1 Asymptotic Giant Branch Stars

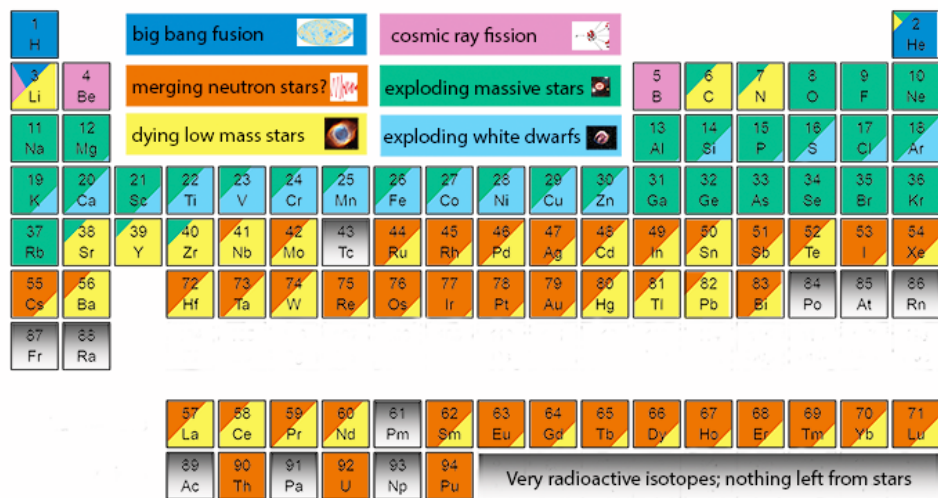
An AGB star is a low mass ($\lesssim 8M_{\odot}$) star during its final phase of evolution. In an AGB star, two competing processes determine the outcome of C production: third dredge up and hot bottom burning. Third dredge up accompanies thermal pulses in AGB stars. During a third dredge up event, material from the CO core is mixed with material exposed to partial He-shell burning, increasing C and O abundances in the envelope (Karakas & Lattanzio 2014). If this envelope is lost during the AGB phase, then C yields are enhanced. hot bottom burning is the activation of proton capture reactions, and the CNO cycle² at the base of the convective envelope. Because the $^{14}\text{N}(\text{p}, \gamma)$ proton capture is the slowest component of the CNO cycle (Adelberger et al. 2011), the CNO cycle converts nearly all ^{12}C into ^{14}N . As a result, when both third dredge up and hot bottom burning, ^{12}C yields are lowered (see discussion in Johnson et al. 2023 and Ventura et al. 2013).

In this work, I explore four different sets of AGB star yield tables from literature, providing well-sampled grids in metallicity and mass for use in chemical evolution

¹VICE is available at <https://github.com/giganano/VICE>

²The CNO (I) cycle is $^{12}\text{C}(\text{p}, \gamma) ^{13}\text{N}(\beta^+ \nu_e) ^{13}\text{C}(\text{p}, \gamma) ^{14}\text{N}(\text{p}, \gamma) ^{15}\text{O}(\beta^+ \nu_e) ^{15}\text{N}(\text{p}, \alpha) ^{12}\text{C}$. Other minor branches of the CNO cycle are of minor importance to C yields (Adelberger et al. 2011).

The Origin of the Solar System Elements



Graphic created by Jennifer Johnson
<http://www.astronomy.ohio-state.edu/~jaj/nucleo/>

Astronomical Image Credits:
 ESA/NASA/AASNova

Figure 2: The periodic table of elements. Taken from Johnson (2019).

models.

- C11: Cristallo et al. (2011, 2015)
- K10: Karakas (2010)
- V13: Ventura et al. (2013, 2014, 2018, 2020)
- K16: Karakas & Lugaro (2016) Karakas et al. (2018)

I use C11table, amplified by a factor of 2.9, as the fiducial AGB yield.

Fig. 3 compares the AGB C yield $\tilde{y}_C^{\text{AGB}}(M, Z)$ for each model I consider. The yields may be negative if a star ejects material with a lower average C abundance than the material the star was formed from. Most models agree on the qualitative shape of the net fractional AGB C yield—stars with masses between $\sim 2 M_\odot$ and $\sim 4 M_\odot$ have the highest fractional C yields, with the mass of the peak increasing and overall yields decreasing with increasing Z . High mass, high Z stars destroy ^{12}C because they experience both third dredge up and hot bottom burning, but the latter is much more efficient.

In Fig. 4, I plot the total production of C by AGB stars in a SSP at an age t . Effectively, this is equivalent to integrating Eq. 2 down to M_{to} , the turnoff mass for time t . (In our model, the mass-lifetime relation is $\log \tau_M = 1.02 - 3.57 \log M + 0.90 (\log M)^2$, where τ_M is in Gyr, from Larson 1974.) As the mass range $2 \lesssim M \lesssim 4$ is most important for C production, about half of C production occurs before ~ 1 Gyr, similar to SNE Ia Fe. K10 and K16 weight C production more heavily towards massive stars resulting in a faster enrichment delay time, whereas the C11 and V13 models predict a slightly longer timescale of ~ 1 Gyr, but little to no C is produced more than 2 Gyr after a star formation event. This is in contrast to Fe whose production lasts up to 10 Gyr after a star formation event. As shown in the right panel of Fig. 4, with increasing Z , C enrichment occurs earlier, and C destruction in low-mass stars leads to a declining C abundance at late times.

Fig. 5 shows IMF-averaged C yields for each AGB model as a function of metallicity Z . V13 differs in that it shows a non-monotonic metallicity dependence. However, this effect is only for models with $\log Z/Z_\odot \lesssim -1$. Otherwise, models differ only in their yield normalization and metallicity dependence. All models predict yields within a factor of ~ 2 for fixed metallicity. For example, the three models C11, K10, and K16 predict y_C^{AGB} to be between 0.006 and 0.008 at solar metallicity, but C11 has a much shallower metallicity dependence than the K10 and K16 models. V13 instead predicts a yield ~ 0.004 .

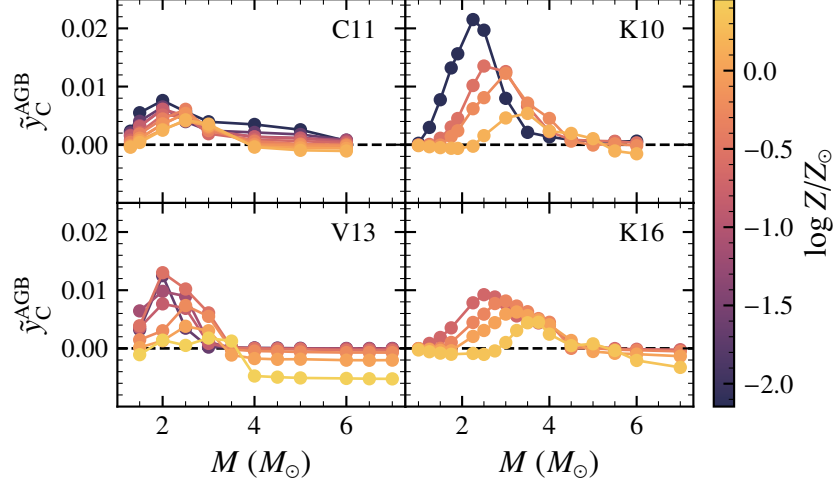


Figure 3: The net fractional AGB C yield plotted as a function of initial stellar mass M and color-coded according to metallicity. The black dashed line shows $\tilde{y} = 0$ for reference. Each panel represents yields from one of four AGB models: C11, K10, V13, K16 (see section 2.1).

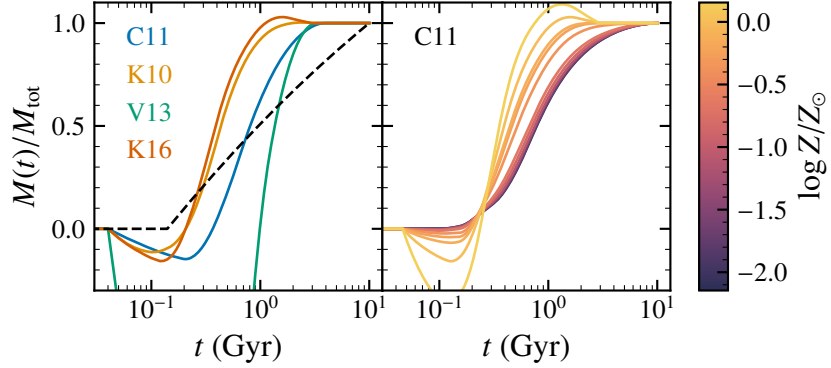


Figure 4: C production by AGB stars as a function of ssp age, normalized to the total mass M_{tot} produced at $t = 10$ Gyr. Left: The four AGB yield models from literature at solar metallicity (C11, K10, V13, or K16). The delay time distribution of type Ia supernovae ($\propto t^{-1.1}$) is plotted as a dashed black line for comparison. Right: The C11 AGB model at different metallicities.

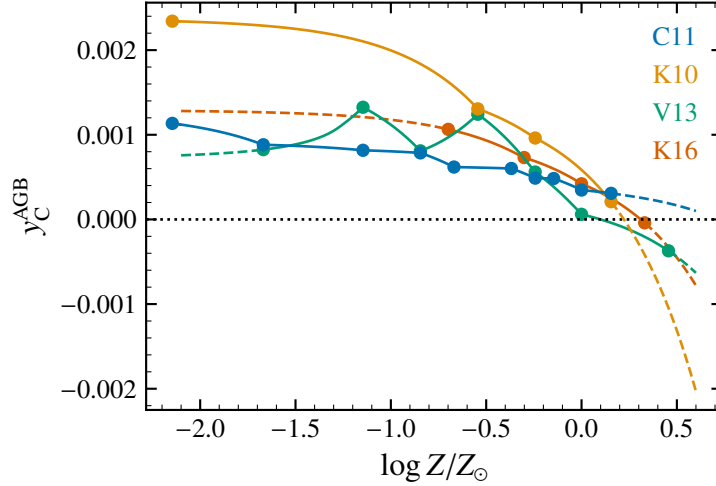


Figure 5: The net fractional IMF-weighted AGB C yield y_C^{AGB} as a function of metallicity for each of our AGB yield models.

2.2 Core Collapse Supernovae

Massive stars form ^{12}C in their cores through the triple- α process. However, only C ejected through supernovae and stellar winds contributes to the yield. While there are many stellar models providing predictions of CCSNE yields, the results of these models are highly uncertain due to the many stellar modeling uncertainties.

In Fig. 6, I plot calculations of the IMF-integrated yields, defined with Eq. 2 (computed using VICE’s `vice.yields.ccsne.fractional` function). CCSNE models predict a wide range of C yields, spanning almost 1 dex. Both the Nomoto et al. (2013) and Limongi & Chieffi (2018) models show positive metallicity dependence. The Limongi & Chieffi (2018) models also include rotation, showing that variations in the rotational velocity of the star can dramatically increase C production and the metallicity dependence of y_C^{CC} . Rotation induces more mixing allowing the CO core to grow larger. Our fiducial model’s steep metallicity dependence near $Z \approx Z_\odot$ could be explained by rotation. Fig. 6 shows the C11 model for comparison on the top. Especially at $Z \approx Z_\odot$, most CCSNE models dominate AGB C production. I will later also show empirically that CCSNE should dominate C production.

On the bottom of Fig. 6, I also show the $\text{ccsne-}[\text{C/Mg}]$ ratio, defined by

$$[\text{C/Mg}]^{\text{cc}} = \log_{10} \left(\frac{y_{\text{C}}^{\text{cc}}}{y_{\text{Mg}}^{\text{cc}}} \right) - \log_{10} \left(\frac{Z_{\text{C}, \odot}}{Z_{\text{Mg}, \odot}} \right). \quad (3)$$

$[\text{C/Mg}]^{\text{cc}}$ describes what $[\text{C/Mg}]$ would be if ccsne were the only process producing C. Once again, different ccsne models span a large range in $[\text{C/Mg}]$. I chose to instead parameterize y_{C}^{cc} to enable agreement with observations, as most ccsne models fail to achieve near-solar $[\text{C/Mg}]$. Assumptions about the explodability landscape affect C and Mg production. Increasing the fraction of stars that explode increases y_{C}^{cc} , as stars that directly collapse do not contribute to explosive yields (Griffith et al. 2021). However, C is relatively unaffected by the black-hole landscape, as very massive stars contribute C through enriched winds. Since Mg is formed deeper in the core of massive stars, the Mg yield drops much more steeply, so models, where few stars explode (S16/W18), result in much higher $[\text{C/Mg}]$.

Ccsne models also do not reach $[\text{O/Mg}]$ due to overproduction of O, or underproduction of Mg, or both (Griffith et al. 2021). Here, I assume $[\text{O/Mg}] = 0$, which is not compatible with ccsne models but is consistent with APOGEE observations (Weinberg et al. 2019, 2022).

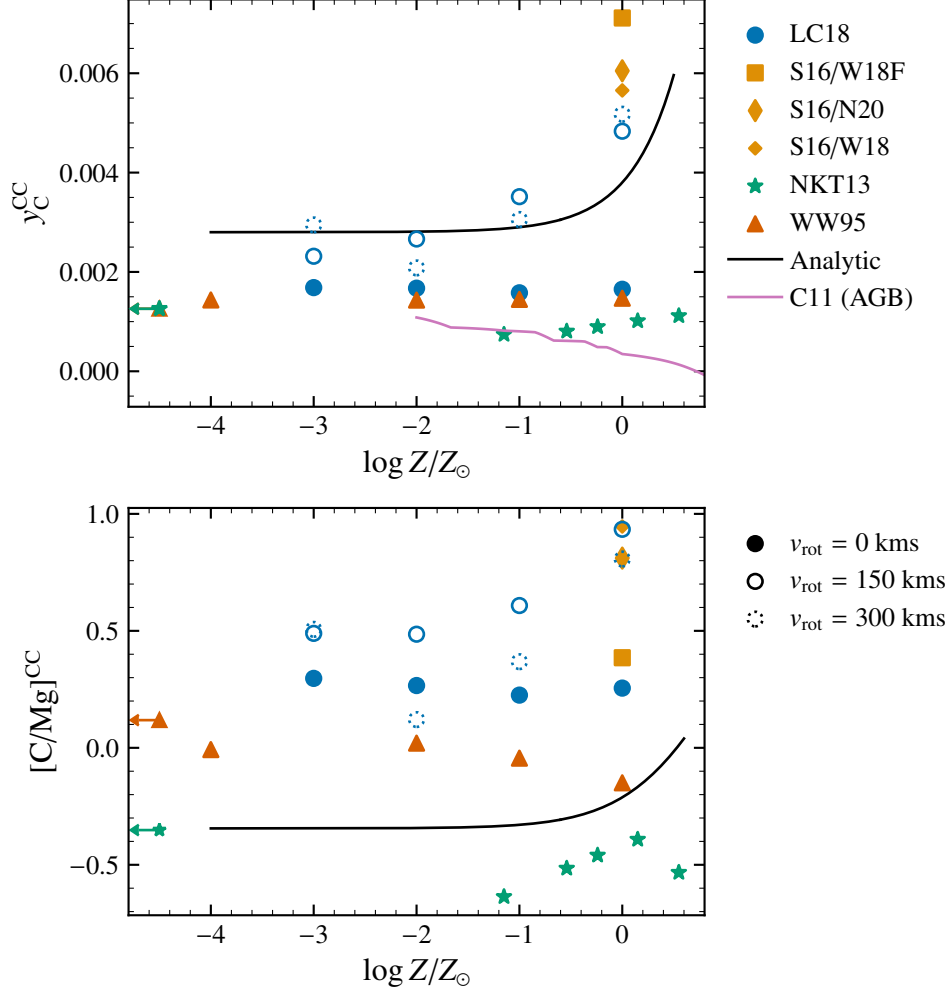


Figure 6: C yields from massive stars. **Top:** The IMF-weighted CCSNE yield of C as a function of metallicity. **Bottom:** The CCSNE [C/Mg] abundance ratio, defined in Eq. 3. The black line represents the C yield of the fiducial model, $y_C^{\text{CC}} = 0.0028 + 0.001(Z/Z_\odot)$. Yields are shown for tables from Woosley & Weaver (1995; red triangles), Sukhbold et al. (2016; orange squares and diamonds), Nomoto et al. (2013; green stars), and Limongi & Chieffi (2018; blue circles). Sukhbold et al. (2016) report yields for different black hole landscapes, while Limongi & Chieffi (2018) provide yields at different rotational velocities. In the top panel, the pink line denotes y_C^{AGB} from C11 for comparison.

3. The Equilibrium Approximation

In the presence of metal-poor gas accretion and feedback-driven outflows, galaxies reach an equilibrium abundance in which production of new metals is balanced by losses to new stars and outflows (Larson 1972; Dalcanton 2007; Finlator & Davé 2008; Peeples & Shankar 2011; Lilly et al. 2013). While our galaxy is likely not in perfect equilibrium or described by a single, homogeneous chemical region, the equilibrium approximation is nevertheless useful in understanding yields and metallicity dependence (e.g. Johnson et al. 2022, 2023; Weinberg et al. 2017).

I assume a simple *one-zone* chemical evolution model (e.g. Tinsley 1980; Pagel 2009; Matteucci 2021). Newly produced metals are homogeneously and instantaneously mixed, so spatial dependence is neglected. I define M_X to be the mass of element X in the gas phase, \dot{M}_\star to be the star formation rate (in $M_\odot \text{ yr}^{-1}$), and η to be the mass loading factor $\eta \equiv \dot{M}_{\text{outflow}}/\dot{M}_\star$ (representing the strength of outflows). SSP's return a fraction r of their birth mass back to the interstellar medium, due to ejected stellar envelopes. ($r \approx 0.4$ for a Kroupa 2001 IMF.) Given the IMF-averaged yield of Mg y_{Mg} , the rate of change in the gas-phase mass of Mg \dot{M}_{Mg} is a simple sum of sources and sinks,

$$\dot{M}_{\text{Mg}} = y_X \dot{M}_\star - \dot{M}_{\text{Mg, remnants}} - \dot{M}_{\text{Mg, outflows}}, \quad (4)$$

where the first term on the right-hand side describes CCSNE enrichment. In terms of the return mass fraction of stars r , the mass lost to remnants is $Z_X(1-r)\dot{M}_\star$. And, the outflows deplete mass at a rate $Z_X\eta\dot{M}_\star$. (I assume the composition of outflows is the same as the interstellar medium.) Substituting for η and r ,

$$\dot{M}_{\text{Mg}} = y_X \dot{M}_\star - (1 + \eta - r)Z_X \dot{M}_\star. \quad (5)$$

Assuming an exponentially declining star formation history $\dot{M}_\star \propto e^{-t/\tau_{\text{sfh}}}$, the equilibrium abundance is derived analytically by setting $\dot{Z}_{\text{Mg}} = 0$.

$$Z_{\text{Mg}}^{\text{eq}}(R) = \frac{y_{\text{Mg}}}{1 + \eta(R) - r - \tau_\star/\tau_{\text{sfh}}}, \quad (6)$$

where τ_\star is the star formation rate. In the special case of constant star formation, $\tau_{\text{sfr}} \rightarrow \infty$, the denominator simplifies to $1 + \eta - r$.

While Equation 6 can be applied to CCSNE C, the delayed nature of AGB C can complicate the expression. Instead, I use an effective yield, which can be expressed as an integral over the delay time distribution,

$$\langle y_C^{\text{AGB}} \rangle = \frac{\int_0^T \tilde{y}_C^{\text{agb}}(M, Z) \dot{M}_\star(T-t) \frac{dN}{dM} \frac{dM}{dt} dt}{\dot{M}_\star \int_0^T \frac{dN}{dM} \frac{dM}{dt} dt}. \quad (7)$$

Eq. 6 then becomes

$$Z_C^{\text{eq}}(R) = \frac{y_C^{\text{CC}} + \langle y_C^{\text{AGB}} \rangle}{1 + \eta(R) - r - \tau_\star / \tau_{\text{sfr}}} \quad (8)$$

And the equilibrium C/Mg abundance ratio is

$$\frac{Z_C^{\text{eq}}}{Z_{\text{Mg}}^{\text{eq}}} = \frac{y_C^{\text{CC}} + \langle y_C^{\text{AGB}} \rangle}{y_{\text{Mg}}^{\text{CC}}}. \quad (9)$$

Analogous to Johnson et al. (2023) arguments about N, the trends in abundance ratios are set by yield ratios in these GCE models. The effect of other GCE parameters (most importantly η) cancels. As a consequence, yield ratios should establish abundance ratio trends in models which assume a different normalization of element yields and mass-loading (see discussion below). This argument can also be inverted to infer yields from abundance ratio trends. To the extent that observed C and Mg trends reflect the equilibrium abundances in different Galactic regions, we can infer the CCSNE yield given an assumed AGB star yield (or vice versa). Inferring y_C^{CC} from y_C^{AGB} ,

$$y_C^{\text{CC}} = y_{\text{Mg}}^{\text{CC}} \frac{Z_{\text{C, eq}}}{Z_{\text{Mg, eq}}} - \langle y_c^{\text{agb}} \rangle \quad (10)$$

Rewriting this expression as a relative yield of C and Mg,

$$\frac{y_C^{\text{CC}}}{y_{\text{Mg}}^{\text{CC}}} = \frac{Z_{\text{C}, \odot}}{Z_{\text{Mg}, \odot}} 10^{[\text{C/Mg}]} - \frac{\langle y_C^{\text{AGB}} \rangle}{y_{\text{Mg}}^{\text{CC}}}. \quad (11)$$

3.1 Yield Models

As I will discuss in section 5.5, the normalization of yields and η is degenerate. This can be observed in Eq. 9, where changes in η or the scaling of y_C/y_{Mg} would

not affect equilibrium trends. Furthermore, in Eq. 6, an increase in both y_{Mg} and η would leave $Z_{\text{Mg}}^{\text{eq}}$ unchanged. My models here are unable to distinguish the overall scaling of yields and outflow mass loading, and choosing to keep y_{C} fixed reduces unnecessary free parameters. As a result, I choose to leave the total C yield fixed at solar Z ,

$$y_{\text{C}} \big|_{Z=Z_{\odot}} = y_{\text{C}}^{\text{CC}} + y_{\text{C}}^{\text{AGB}} = 0.005 \quad (12a)$$

$$y_{\text{C}}/y_{\text{Mg}}^{\text{CC}} \big|_{Z=Z_{\odot}} = 2.7. \quad (12b)$$

This ratio results in an equilibrium abundance $[\text{C}/\text{Mg}] = -0.09$, which is consistent with the Roberts et al. (2023, in prep.) subgiant sample and is within $\sim 20\%$ of the solar C/Mg mixture from Asplund et al. (2009).

In section 5.3, I will show that none of the four AGB yield sets (C11, K10, V13, K16) produce enough C relative to this y_{C}^{CC} value. So, I introduce normalization factors, α_{AGB} , and α_{CC} which denote a multiplicative scaling of y_{C}^{CC} and $y_{\text{C}}^{\text{AGB}}$ respectively.

$$y_{\text{C}}^{\text{AGB}} \rightarrow \alpha_{\text{AGB}} (y_{\text{C}}^{\text{AGB}}) \quad (13a)$$

$$y_{\text{C}}^{\text{CC}} \rightarrow \alpha_{\text{CC}} (y_{\text{C}}^{\text{CC}}) \quad (13b)$$

$$\alpha_{\text{CC}} = \frac{y_{\text{C}} - \alpha_{\text{AGB}} (y_{\text{C}}^{\text{AGB}})}{y_{\text{C}}^{\text{CC}}} \quad (13c)$$

Above, α_{CC} is dependent on the choice of α_{AGB} to keep the total C yield constant.

In section 5.3, I find that $\alpha_{\text{AGB}} \approx 2.9$ for the C11 yield model. Using this AGB yield, I can now use Eq. 11 to find an estimate of y_{C}^{CC} as a function of metallicity. I show the values of y_{C}^{CC} I obtain from the subgiant sample in Fig. 7. From regression analysis, I suggest here that

$$y_{\text{C}}^{\text{CC}} = 0.0028 + \zeta \left(\frac{Z}{Z_{\odot}} \right), \quad (14)$$

where ζ , describing the metallicity dependence, is $\zeta \approx 0.001$.

3.2 Uncertainties

I only perform this analysis on the C11 yields because C11 has yields tables more finely sampled in metallicity than the other three AGB yield tables. As the metallicity range of the data is small ($-0.4 \lesssim [\text{Mg}/\text{H}] \lesssim 0.4$), other models are

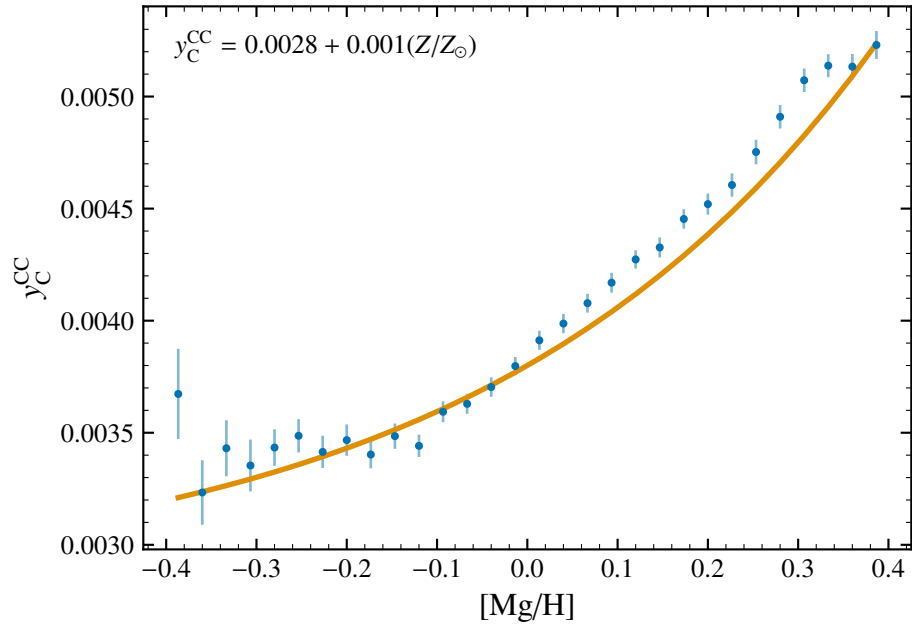


Figure 7: Inferred massive star C yields as a function of metallicity. I assume equilibrium and $3 \times \text{C11}_{\text{AGB}}$ yields (orange curve, see discussion in Section 3). The binned medians and median absolute deviation (divided by \sqrt{N}) are blue points.

more challenging to interpret in this range. Furthermore, the APOGEE observations may have systematics, and other measurements of C abundances (e.g. Vincenzo et al. 2021) have slight disagreements in the overall shape of the trend (see section A.1). So, this expression of $y_C^{\text{CC}}/y_{\text{Mg}}^{\text{CC}}$ depends on the chosen AGB yield table, the AGB fraction, and the dataset. Additionally, these yields will be systematically biased if the galaxy is out of equilibrium, for example due to a recent starburst (Isern et al. 19; Mar et al. 19). Further exploration could investigate the magnitude of these uncertainties, but I find that the qualitative conclusions are similar despite substantial variations in the assumptions here.

4. The Multizone Model

Classical, *one-zone* models of chemical evolution assume instantaneous mixing of metals in the star-forming interstellar medium (e.g. Matteucci 2021). This simple framework is a poor approximation for the Milky Way. The Galaxy evolves “inside out”—where star formation is higher towards the center and in the early universe (Bird et al. 2013). Additionally, stars can migrate several kpc over their lifetimes, mixing together different chemical environments across the galaxy (Bird et al. 2012; Sellwood & Binney 2002). For the rest of this paper, I focus on multi-zone models, which discretize the Galaxy into concentric annuli and allow stars to move between rings. Specifically, I make use of the Johnson et al. (2021) (hereafter J21) model for the Milky Way, which runs using the publicly available Versatile Integrator for Chemical Evolution (VICE). This model is described extensively in J21 and concisely summarized in Johnson et al. (2023). Here, I provide a brief overview of the relevant model components.

In the model, the Galaxy is divided into 200 rings, each 100 pc wide. Each ring has a separate stellar population and gas supply. Star formation ends beyond a radius $R = 15.5$ kpc. I initially assume an “inside-out” SFH, where the star formation surface density Σ_\star is given by

$$\dot{\Sigma}_\star \propto \left(1 - e^{-t/\tau_{\text{rise}}}\right) e^{-t/\tau_{\text{sff}}}. \quad (15)$$

$\tau_{\text{rise}} = 2$ Gyr describes when the star formation rate reaches a maximum, and τ_{sff} describes the decay timescale of star formation as a function of radius R . J21 derives $\tau_{\text{sff}}(R)$ through analysis of four integral field spectroscopy surveys in Sánchez (2020). The star formation history is normalized such that the total stellar mass reaches $M_\star = 5.17 \times 10^{10} M_\odot$ (Licquia & Newman 2015) and at each R to match the stellar surface density gradient (Bland-Hawthorn & Gerhard 2016). The gas inflow is calculated to maintain our chosen SFH for each radius and time. The gas-SFR law is based on an extension of a Kennicutt-Schmidt law (Kennicutt

1998), motivated by

$$\dot{\Sigma}_\star \propto \begin{cases} \Sigma_{\text{gas}} & 2 \times 10^7 \leq \Sigma_{\text{gas}} \\ (\Sigma_{\text{gas}})^{3.6} & 5 \times 10^6 \leq \Sigma_{\text{gas}} < 2 \times 10^7 \\ (\Sigma_{\text{gas}})^{1.7} & \Sigma_{\text{gas}} < 5 \times 10^6 \end{cases} \quad (16)$$

The scaling of this relationship varies with time due to the redshift dependence of τ_\star in molecular gas observed by Tacconi et al. (2018). I assume a Kroupa IMF Kroupa (2001).

J21 accounts for radial migration by using the results of the h277 hydrodynamical simulation (Christensen et al. 2012; Zolotov et al. 2012; Loebman et al. 2012; Brooks & Zolotov 2014), with simulation parameters described in Bird et al. (2021). Each VICE single stellar population (SSP) is matched to an *analog* in H277, chosen to form at a similar time and radius R . By taking the change in radius ΔR of the analogs, the ssp move to their final radii with a $\sqrt{\text{time}}$ dependence. This relationship between displacement and time arises when migration proceeds as a consequence of the diffusion of angular momentum (Frankel et al. 2018, 2020). I do not account for radial gas flows. Using the results of a hydrodynamical simulation without modification limits the free parameters in the model; however, I am limited to one dynamical history. The impact of the details of a galaxy’s dynamical history on its chemical evolution is unknown, and I do not explore this question here.

As the strength of outflows controls the resulting α abundances, J21 create a metallicity gradient by defining

$$\eta(R) = \frac{y_\alpha^{\text{CC}}}{Z_{\alpha,\odot}} 10^{(-0.08 \text{ kpc}^{-1})(R-4 \text{ kpc})+0.3} + r - 1. \quad (17)$$

This choice of $\eta(R)$ results in a $[\alpha/\text{H}]$ gradient consistent with Milky Way observations (e.g. Hayden et al. 2014; Weinberg et al. 2019; Frinchaboy et al. 2013).

5. Multizone Model Results

5.1 Data Selection

Johnson et al. (2023) compare their model against the Vincenzo et al. (2021) sample of APOGEE (Majewski et al. 2017) red giant branch C and N abundance have been corrected for mixing process using MESA stellar evolution models. I instead use the Roberts et al. (2023, in prep.) sample of APOGEE subgiants. Subgiant stars have not undergone first dredge up but have well mixed atmospheres, so their atmospheric C and N abundances are still reflective of their birth abundances and do not need mixing corrections. I additionally only compare the models to the low- α sequence. The selection criteria and differences between the samples are described in more detail in Appendix A.1.

5.2 The Evolution of C Abundances in the Galaxy

Here, I present the time evolution of our fiducial model. In the next sections, I will discuss the choice of parameters and agreement with observations. The fiducial model has the following qualitative characteristics of its C yields: (a) C is predominantly produced in CCSNE, (b) CCSNE produce more C at higher metallicities, and (c) AGB stars produce less C at higher metallicities. Our fiducial model uses the C11 AGB yield tables (see section 2.1, and Table 1), and I amplify the C11 yields by a factor of 2.9 such that AGB stars account for 20% of C at $Z = Z_{\odot}$.

I show the time evolution tracks of the fiducial model in Fig. 8 for $[C/Mg]$ - $[Mg/H]$ and $[C/Mg]$ - $[Mg/Fe]$. Comparing $[C/Mg]$ against $[Mg/Fe]$ enables us to see the late-time evolution of C more clearly. Because of the extended delay time distribution of SNE Ia enrichment, $[Fe/H]$ takes longer to reach equilibrium as half of Fe production comes from type-Ia supernovae, and the late time evolution is not as clustered as $[Mg/H]$. The evolution proceeds as follows. Initially, CCSNE dominate production. As y_C^{CC} has strong metallicity dependence, $[C/Mg]$ increases with time. Shortly thereafter, AGB stars contribute delayed C, increasing $[C/Mg]$

even more steeply. As Mg begins to reach equilibrium, the [C/Mg] ratio plateaus as C approaches equilibrium. Finally, as y_C^{AGB} decreases or even becomes negative with higher metallicity, the [C/Mg] abundance may decline slightly. This is even more evident in the lower panel of Fig. 8. While the [C/Mg]-[Mg/H] trend reaches equilibrium at ~ 5 Gyr, the [C/Mg]-[Mg/Fe] trend continues to evolve even until the present day, exposing the effect of the relative delay times of AGB stars and SNE IA.

5.3 Alternate Models

Fig. 9 compares the K10, K16, C11, and V13 yield models. Here, I use the published, unscaled yield tables. As the highest AGB yield at solar, K10 is only $y_C^{\text{AGB}} = 0.000585$, $f_{\text{AGB}} \leq 0.12$ for all models. Massive stars dominate C production with unscaled yields. While it is easy to modify the AGB yields in my model, their small contribution reduces the effect. I leave a more detailed discussion of the effects of AGB models for Appendix A.2 and use C11 yields hereafter.

Next, I investigate adjustments to the AGB yield fraction f_{AGB} and the CCSNE metallicity dependence ζ in Fig. 10. On the top panel of Fig. 10, I plot models with varying y_C^{CC} metallicity dependence. As discussed in section 3, the [C/Mg]-[Mg/H] trend is approximated by equilibrium, so the trends of these have steeper [C/Mg]-[Mg/H] corresponding to steeper metallicity dependence. However, [C/Mg]-[Mg/Fe] is minimally affected by these changes since CCSNE occur on much shorter timescales than SNE IA and AGB enrichment.

Now, I vary the proportion of AGB contribution. The AGB C production fraction is defined as

$$f_{\text{AGB}} \equiv \frac{y_C^{\text{AGB}}}{y_C} \bigg|_{Z=Z_\odot}, \quad (18)$$

where y_C^{AGB} includes the multiplicative factor α_{AGB} as defined in Eq. 13. In the bottom panel of Fig. 10, I plot three models with different AGB fractions while using C11 yields. The [C/Mg]-[Mg/Fe] relationship is set by f_{AGB} because a specific amount of C must be released at a delayed time in order to match the SNE IA production of Fe and increase [C/Mg] as [Mg/Fe] decreases to reproduce the data. Increased f_{AGB} results in a decreased slope in [C/Mg]-[Mg/H], owing to the negative metallicity dependence of y_C^{AGB} . So while [C/Mg]-[Mg/H] alone cannot differentiate models which vary f_{AGB} and ζ correspondingly, [C/Mg]-[Mg/Fe] provides information on f_{AGB} . So, I can use [C/Mg]-[Mg/Fe] to estimate $f_{\text{AGB}} \approx 0.2$, and then choose ζ in order to match [C/Mg]-[Mg/H].

One source of theoretical uncertainty in this result is that the SNE IA yield and

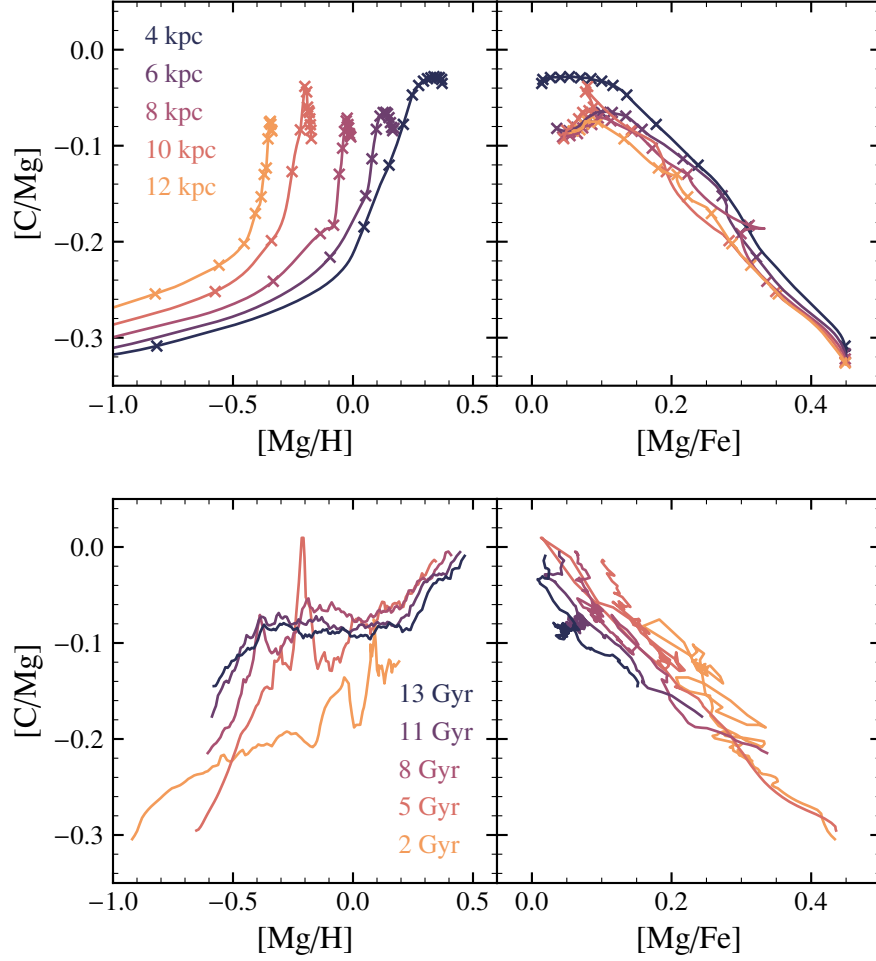


Figure 8: Time evolution of gas phase C abundances in our fiducial model. **Top:** Evolutionary tracks parameterized by time at fixed Galactocentric radius in the [C/Mg]-[Mg/H] and [C/Mg]-[Mg/Fe] planes. **Bottom:** snapshots of the gas-phase [C/Mg]-[Mg/H] and [C/Mg]-[Mg/Fe] trend, parameterized by radius at a fixed time.

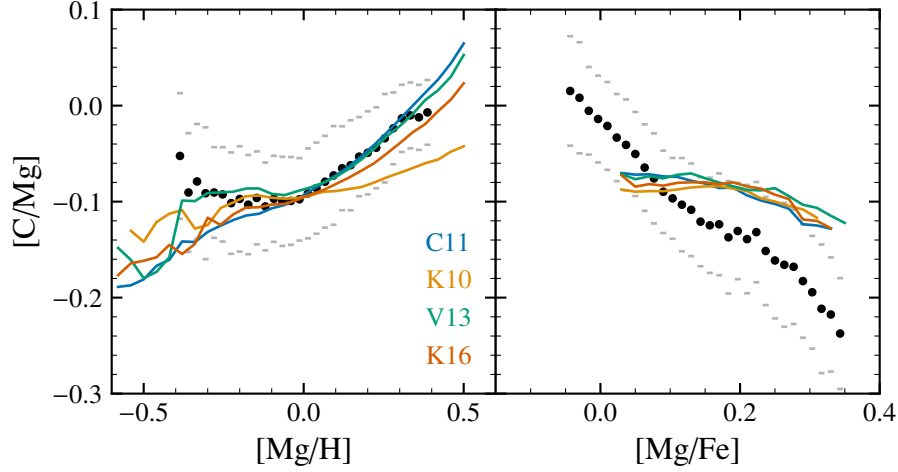


Figure 9: Stellar abundance trends in our model, assuming metallicity independent y_C^{CC} . Colored lines quantify the median $[C/Mg]$ in bins of $[Mg/H]$ for our four AGB yield models from the literature (see 2.1). Black points and grey dashes represent the median and standard deviations in the Roberts et al. (2023, in prep.) sample. In the right panel, I show the trends only for stars where $-0.15 \leq [Mg/H] \leq -0.05$.

delay time distributions have their own uncertainties. I discuss variations in $y_{\text{Fe}}^{\text{Ia}}$ in Appendix A.2, and find that the qualitative conclusions are largely unaffected. I therefore focus on the choices of $y_{\text{Fe}}^{\text{Ia}} = 0.00214$ and a $\propto t^{-1.1}$ delay time distribution choices from the fiducial model here. In short, the scaling of the trend and metallicity dependence of C (as seen in the $[C/Mg]$ - $[Mg/H]$ trend) gives information on the total C yield and the behavior of CCSNE (as the dominating producer of C), the $[C/Mg]$ - $[Mg/Fe]$ trend exposes the delayed effect of C from AGB contribution.

5.4 Star Formation History

Here, I consider a "lateburst" model, created by multiplying our fiducial "inside-out" SFH with a Gaussian.

$$\dot{\Sigma}_{\text{lateburst}} \propto \dot{\Sigma}_{\text{insideout}} \left(1 + A e^{-(t-\tau_{\text{burst}})^2/2\sigma_{\text{burst}}^2} \right) \quad (19)$$

$A = 1.5$ represents the amplitude of the birth, $\tau_{\text{burst}} = 10.8\text{Gyr}$ is the time where the burst is strongest, and $\sigma_{\text{burst}} = 1\text{Gyr}$ is the width of the burst.

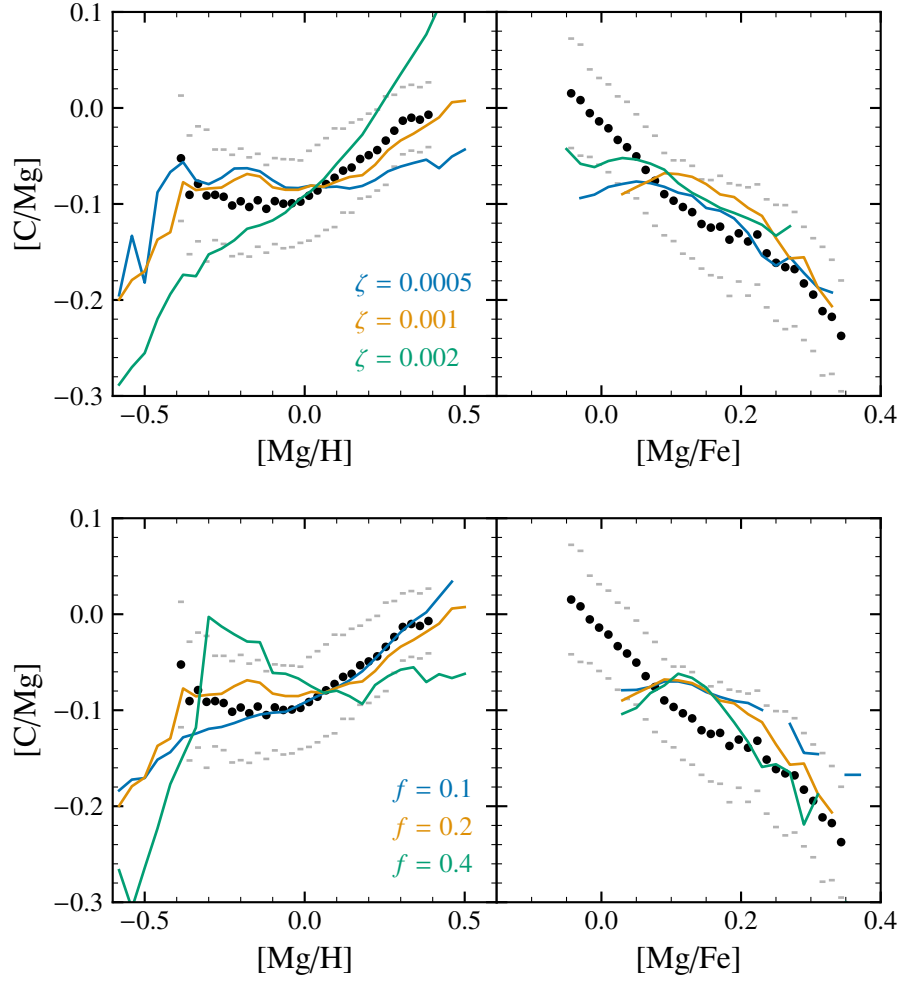


Figure 10: Similar to Fig. 9 except the top plot shows the fiducial model with lower and higher values of ζ , the metallicity dependence of y_C^{CC} . The bottom plot shows models with $f_{AGB} = 0.1, 0.2$, and 0.4 . Both the f_{AGB} and ζ influence $[C/Mg]$ - $[Mg/H]$, but only f_{AGB} has a significant impact on $[C/Mg]$ - $[Mg/Fe]$.

Table 2: For each AGB yield set, the IMF-weighted C AGB yield at solar metallicity, along with the multiplicative factor reaches an AGB contribution of 20%.

| AGB Model | $y_{\text{C},0}^{\text{AGB}}$ | $\alpha_{\text{AGB},20}$ |
|-----------|-------------------------------|--------------------------|
| C11 | 0.000347 | 2.9 |
| K10 | 0.000585 | 1.7 |
| V13 | 0.000060 | 16.5 |
| K16 | 0.000421 | 2.4 |

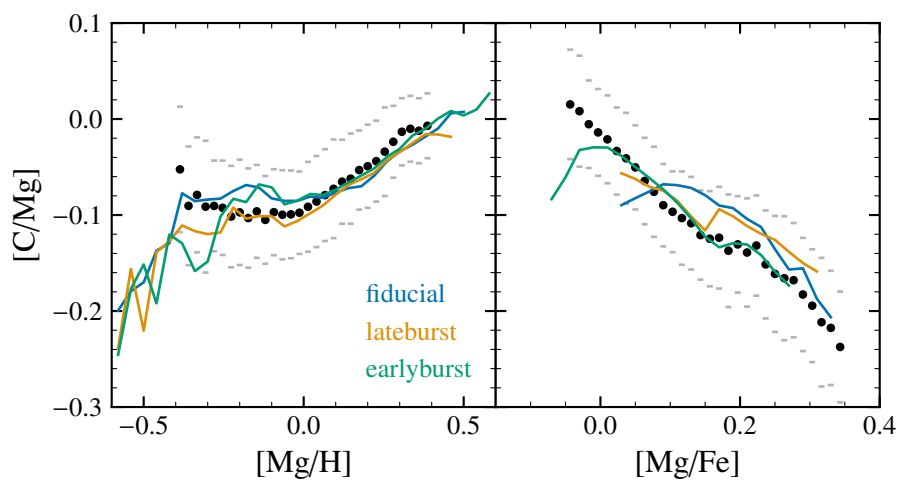


Figure 11: Same as Fig. 9 but comparing the fiducial model to alternate SFHS (see section 5.4).

I also consider an earlyburst model as a slight variation of the lateburst, where the burst is instead exponential and placed at $t_1 = 5$ Gyr.

$$\dot{\Sigma}_{\text{early-burst}} \propto \dot{\Sigma}_{\text{insideout}} + \begin{cases} Ae^{-(t-t_1)/\tau_{\text{burst}}} & t_1 < t \\ 0 & t < t_1 \end{cases} \quad (20)$$

where I take the burst duration, $\tau_{\text{burst}} = 1$ Gyr in this case. This approximately corresponds to the Gaia-Encelidus merger, inducing higher star formation in the Milky Way (Spitoni et al. 2021; Bonaca et al. 2020; Helmi et al. 2018).

Fig. 11 shows three models with these alternate SFH. Changes to the SFH leave $[\text{C}/\text{Mg}]-[\text{Mg}/\text{H}]$ unchanged, but they do introduce slight variation in $[\text{C}/\text{Mg}]-[\text{Mg}/\text{Fe}]$. Models with higher AGB fractions are more sensitive to variations in SFH. The late burst models result in $[\text{C}/\text{Mg}]$ continuing to increase at low $[\text{Mg}/\text{Fe}]$, but also introduce a break not present in the data. Additionally, the early burst is able to reproduce the slight break between the low and high α sequences, but overshoots equilibrium more severely than the fiducial model. The choice of SFH does not change the large-scale slope of $[\text{C}/\text{Mg}]-[\text{Mg}/\text{Fe}]$ significantly, so variations of SFH only have minimal effect on my conclusions.

5.5 Outflows

GCE models of the Milky Way fall into two classes—those which incorporate significant mass-loading (e.g., as in this work) and those which neglect mass-loading but lower effective yield to match observed abundances (Minchev et al. 2013, 2014; Spitoni et al. 2019, 2020, 2021). An increase in stellar yields has a nearly identical effect as a decrease in the mass-loading factor η (see Appendix B of Johnson et al. (2022)). The equilibrium arguments discussed in section 3 suggest however that abundance ratios are independent of the choice of normalization and the value of η . I therefore expect my results regarding the relative yield $y_{\text{C}}/y_{\text{Mg}}$ and its metallicity dependence to extend to the other class of models omitting mass loading. I demonstrate this further here.

The theoretical motivation for decreasing yields is the uncertainty in stellar explodability. If fewer massive stars explode, then the yields will be reduced by some factor. Additionally, some fraction of SN ejecta may be lost directly to an outflow, lowering effective yields. To explore reduced outflow models, I lower both η and all yields by the same factor to leave the equilibrium abundances unchanged.

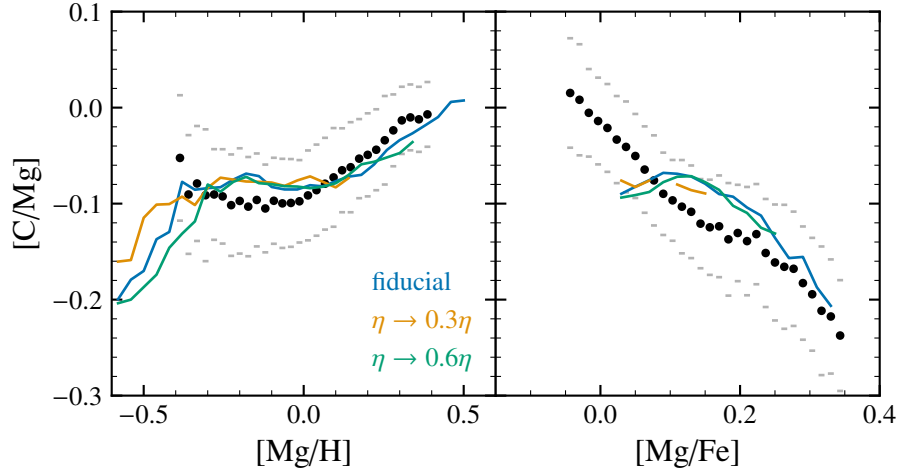


Figure 12: Same as Fig. 9 but comparing the fiducial model to reduced outflow models (see section 5.5).

5.6 Scatter

Median trends have limitations as they do not consider the actual distribution of $[C/Mg]$ - $[Mg/H]$ abundances. So, I show in Fig. 13 a comparison of the predicted distribution of the model to the contours of the subgiant sample. Our model reproduces this 2-dimension distribution well when including scatter based on the median APOGEE abundance errors for each metallicity bin. Some of the scatter is due to radial migration, but observational errors are dominant. Precision abundance measurements will allow tighter constraints on chemical yields.

5.7 Gas-Phase C Abundances

As an additional test of the model, I next compare the gas-phase predictions against gas-phase C data. In Fig. 15, I plot our fiducial model's gas phase predictions compared to observations of MW and extragalactic HII regions, halo stars, and DLA systems. The model is broadly consistent with observations, where the model at $t = 2$ Gyr approximates the slope of dwarf galaxies and halo stars. The increase of C/O at late times is also consistent with the high C/O abundances measured in extragalactic HII regions. My model does not extend to very low metallicity, where the trend reverses, but broadly explains observations above $[O/H] \sim -1$.

Stellar measurements of Mg are more reliable, but O abundances are easier

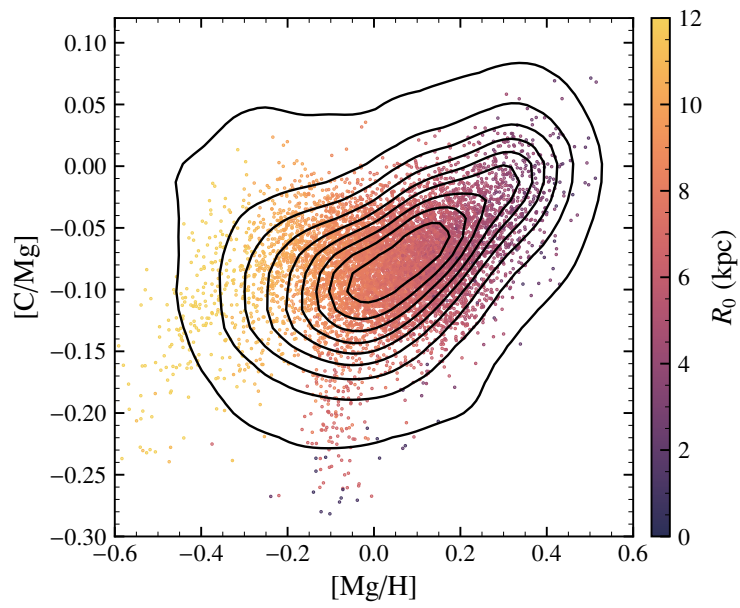


Figure 13: The stars in the fiducial model in the $[C/Mg]$ - $[Mg/H]$ plane perturbed by the median $[Mg/H]$ and $[C/Mg]$ measurement errors in the Roberts et al. (2023, in prep.) sample. Stars are color-coded such that lighter colors represent populations born at greater galactocentric radii

to measure in HII regions. I therefore use Mg abundances from the Roberts et al. (2023, in prep.) subgiant sample as my primary empirical constraint. However, I use O abundances for gas-phase measurements and low-metallicity stars (section 5.7). I model both Mg and O as metallicity-independent population-averaged yields dominated by massive stars. $[O/Mg] \approx 0$ across a wide range of metallicities in APOGEE (Weinberg et al. 2019, 2022). I adopt O and Mg relative yields given by the solar mixture of Asplund et al. (2009).

C/O gas-phase measurements are hard. In HII-regions, C/O abundance ratios are measured with either recombination lines or collisionally excitation lines. However C lacks strong collisional excitation lines, and recombination lines fall in the ultraviolet without nearby reference H lines (Skillman et al. 2020). Additionally, recombination and collisionally excitation measurements disagree by a factor of ~ 2 (García-Rojas & Esteban (2007)). Additional to measurement errors, variations in SFH may explain the scatter, as C contains delayed enrichment, and bursts cause variations in C/O.

The decreasing $[C/O]$ abundance at very-low metallicities is likely due to population III stellar yields (e.g. Hirschi 2007), as suggested by (Cooke et al. 2017; Frebel & Norris 2015). As AGB stars do have a significant delay, these stars cannot explain the increase in C yields at low metallicity as the timescales to reach $[O/H] \sim -1$ is faster than this enrichment can occur. So, enhanced C due to (rotating) massive population III stars at low metallicities explains this trend.

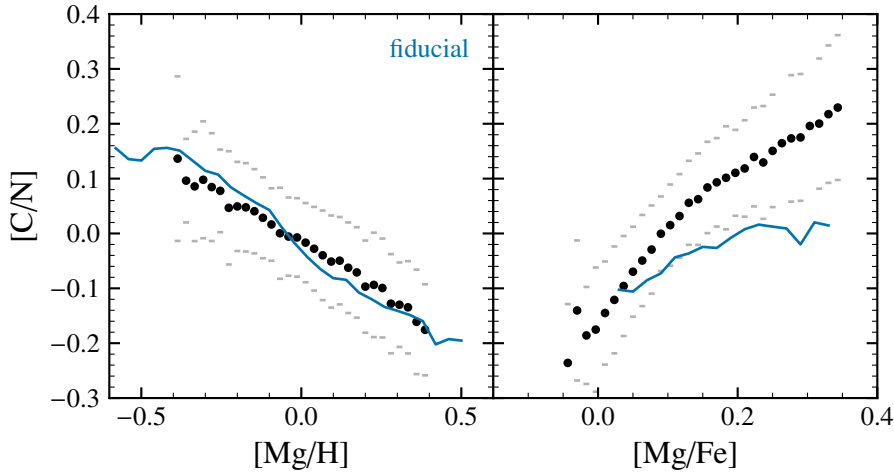


Figure 14: Similar to Fig. 9, except comparing $[C/N]$ from the fiducial model only.

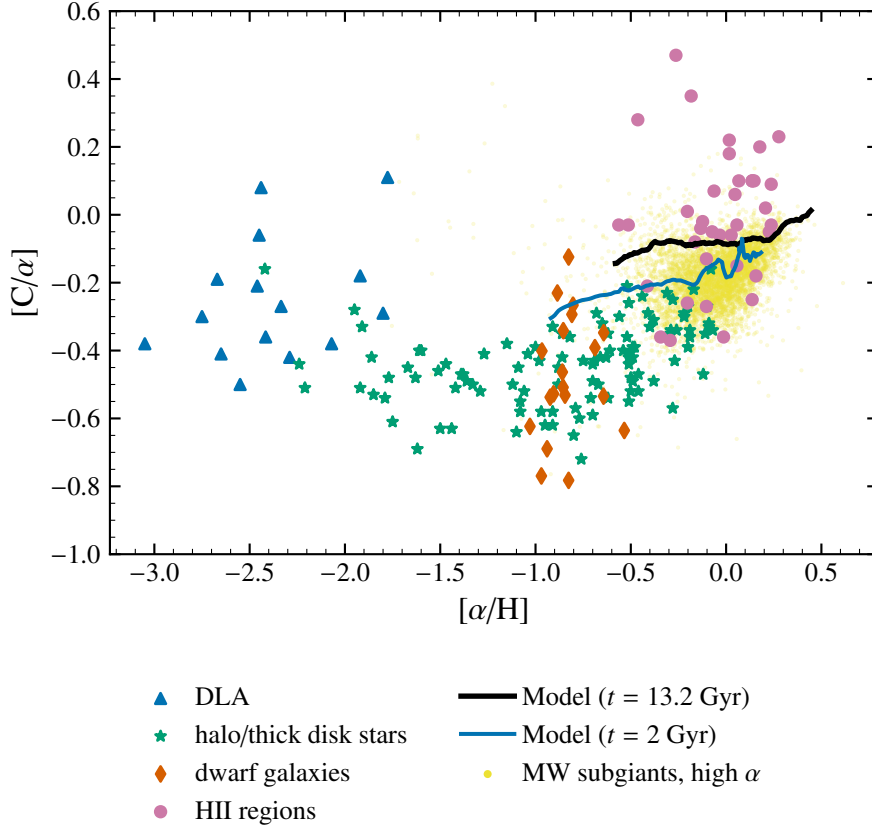


Figure 15: Gas-phase C abundances. We plot our model at $t = 2$ Gyr and present day as thick solid lines. Points represent measurements in HII regions (pink circles; Skillman et al. 2020; Esteban et al. 2002, 2009, 2014, 2019) DLA systems (blue triangles; Ellison et al. 2010; Srianand et al. 2010; Dutta et al. 2014; Dessauges-Zavadsky et al. 2003; Pettini et al. 2008; Morrison et al. 2016; Cooke et al. 2017) Milky Way halo and thick disk stars (green stars; Nissen et al. 2014; Fabbian et al. 2009). dwarf galaxies (Berg et al. 2019; red diamonds;), and Milky Way high- α stars (yellow points; Robert et al. 2023, in prep.)

6. Conclusions

In this work, I investigate the role of C yields on the predictions of multi-zone GCE models. Johnson et al. (2023) performed a similar analysis focusing on N. They found that matching the observed relationship between N and O abundances (Henry et al. 2000; Pilyugin et al. 2010; Berg et al. 2012, 2020; Skillman et al. 2020; Izotov et al. 2012; James et al. 2015; Dopita et al. 2016) requires relative N and O yields from simple stellar populations with a roughly linear dependence on metallicity (i.e. $y_N/y_O \propto Z$). Here, I perform a similar analysis on C.

Though CCSNE C yields are poorly understood, I adopt an equilibrium approximation and determine a functional form that approximately matches trends in APOGEE subgiant and is consistent with massive star nucleosynthesis models. Variations of the metallicity dependence of this CCSNE yield affect trends in $[C/Mg]$ - $[Mg/H]$ but do not affect trends in $[C/Mg]$ - $[Mg/Fe]$ when taking a slice in $[Mg/H]$. As all theoretical AGB C yields decrease with metallicity, increasing the AGB fraction causes the $[C/Mg]$ - $[Mg/H]$ trend to flatten. However, the $[C/Mg]$ - $[Mg/Fe]$ trend is sensitive to the AGB fraction. From this, I estimate that AGB stars contribute $\sim 20\%$ of total C abundance at solar metallicity. The remaining $\sim 80\%$ of C comes from massive stars with a metallicity dependent yield of $y_C^{CC}/y_{Mg}^{CC} = 1.51 + 0.54(Z/Z_\odot)$. This metallicity dependence is consistent with the rotating stellar models of Limongi & Chieffi (2018).

I additionally explore variations of the assumed SFH and outflow mass-loading factor η . I find that alternate SFHs can slightly affect $[C/Mg]$ - $[Mg/Fe]$, but $[C/Mg]$ - $[Mg/H]$ is mostly unaffected. Decreasing both outflows and yields by the same factor leaves the $[C/Mg]$ - $[Mg/H]$ and $[C/Mg]$ - $[Mg/Fe]$ trends unaffected. These constraints on the relative yields of C, O, and Mg are robust against variations in η .

Finally, I compare my model against gas phase measurements and metal-poor stars. While my model was built on data near solar metallicity, observations of very low metallicity, high redshift damped Lyman- α systems indicate higher C/O ratios (Cooke et al. 2017), consistent with yields from population III stars (e.g. Hirschi 2007). Our combined results self-consistently explain C abundances.

These C yield constraints provide a useful benchmark for stellar evolution models. C yields are sensitive to poorly understood processes, including mass loss prescriptions, explodability, nuclear cross sections, convection, and stellar structure. Future spectroscopic surveys combined with Gaia kinematics (Gaia Collaboration et al. 2016) will continue to enhance our understanding of chemical evolution. Both the Sloan Digital Sky Survey V's Milky Way Mapper program (SDSS-V/MWM) (Kollmeier et al. 2017) and the Dark Energy Spectroscopic Instrument (DESI) Milky Way survey (DESI Collaboration et al. 2016; Cooper et al. 2022) will each measure spectra of > 6 million Milky Way stars. These larger samples will enable similar work to tighten constraints on stellar models and our understanding of galaxy structure and evolution.

Bibliography

- Abdurro'uf, Accetta, K., Aerts, C., et al. 2022, *ApJS*, 259, 35, doi: 10.3847/1538-4365/ac4414
- Adelberger, E. G., García, A., Robertson, R. G. H., et al. 2011, *Reviews of Modern Physics*, 83, 195, doi: 10.1103/RevModPhys.83.195
- Asplund, M., Grevesse, N., Sauval, A. J., & Scott, P. 2009, *ARA&A*, 47, 481, doi: 10.1146/annurev.astro.46.060407.145222
- Astropy Collaboration, Robitaille, T. P., Tollerud, E. J., et al. 2013, *A&A*, 558, A33, doi: 10.1051/0004-6361/201322068
- Astropy Collaboration, Price-Whelan, A. M., Sipőcz, B. M., et al. 2018, *AJ*, 156, 123, doi: 10.3847/1538-3881/aabc4f
- Astropy Collaboration, Price-Whelan, A. M., Lim, P. L., et al. 2022, *ApJ*, 935, 167, doi: 10.3847/1538-4357/ac7c74
- Berg, D. A., Erb, D. K., Henry, R. B. C., Skillman, E. D., & McQuinn, K. B. W. 2019, *ApJ*, 874, 93, doi: 10.3847/1538-4357/ab020a
- Berg, D. A., Pogge, R. W., Skillman, E. D., et al. 2020, *ApJ*, 893, 96, doi: 10.3847/1538-4357/ab7eab
- Berg, D. A., Skillman, E. D., Marble, A. R., et al. 2012, *ApJ*, 754, 98, doi: 10.1088/0004-637X/754/2/98
- Bird, J. C., Kazantzidis, S., & Weinberg, D. H. 2012, *MNRAS*, 420, 913, doi: 10.1111/j.1365-2966.2011.19728.x
- Bird, J. C., Kazantzidis, S., Weinberg, D. H., et al. 2013, *ApJ*, 773, 43, doi: 10.1088/0004-637X/773/1/43

- Bird, J. C., Loebman, S. R., Weinberg, D. H., et al. 2021, MNRAS, 503, 1815, doi: 10.1093/mnras/stab289
- Bland-Hawthorn, J., & Gerhard, O. 2016, ARA&A, 54, 529, doi: 10.1146/annurev-astro-081915-023441
- Bonaca, A., Conroy, C., Cargile, P. A., et al. 2020, ApJ, 897, L18, doi: 10.3847/2041-8213/ab9caa
- Brooks, A. M., & Zolotov, A. 2014, ApJ, 786, 87, doi: 10.1088/0004-637X/786/2/87
- Christensen, C., Quinn, T., Governato, F., et al. 2012, MNRAS, 425, 3058, doi: 10.1111/j.1365-2966.2012.21628.x
- Cooke, R. J., Pettini, M., & Steidel, C. C. 2017, MNRAS, 467, 802, doi: 10.1093/mnras/stx037
- Cooper, A. P., Koposov, S. E., Allende Prieto, C., et al. 2022, arXiv e-prints, arXiv:2208.08514, doi: 10.48550/arXiv.2208.08514
- Cristallo, S., Straniero, O., Piersanti, L., & Gobrecht, D. 2015, ApJS, 219, 40, doi: 10.1088/0067-0049/219/2/40
- Cristallo, S., Piersanti, L., Straniero, O., et al. 2011, ApJS, 197, 17, doi: 10.1088/0067-0049/197/2/17
- Dalcanton, J. J. 2007, ApJ, 658, 941, doi: 10.1086/508913
- DESI Collaboration, Aghamousa, A., Aguilar, J., et al. 2016, arXiv e-prints, arXiv:1611.00036, doi: 10.48550/arXiv.1611.00036
- Dessauges-Zavadsky, M., Péroux, C., Kim, T. S., D’Odorico, S., & McMahon, R. G. 2003, MNRAS, 345, 447, doi: 10.1046/j.1365-8711.2003.06949.x
- Dopita, M. A., Kewley, L. J., Sutherland, R. S., & Nicholls, D. C. 2016, Ap&SS, 361, 61, doi: 10.1007/s10509-016-2657-8
- Dutta, R., Srianand, R., Rahmani, H., et al. 2014, MNRAS, 440, 307, doi: 10.1093/mnras/stu260
- Ellison, S. L., Prochaska, J. X., Hennawi, J., et al. 2010, MNRAS, 406, 1435, doi: 10.1111/j.1365-2966.2010.16780.x

- Esteban, C., Bresolin, F., Peimbert, M., et al. 2009, *ApJ*, 700, 654, doi: 10.1088/0004-637X/700/1/654
- Esteban, C., García-Rojas, J., Arellano-Córdova, K. Z., & Méndez-Delgado, J. E. 2019, arXiv e-prints, arXiv:1905.10129. <https://arxiv.org/abs/1905.10129>
- Esteban, C., García-Rojas, J., Carigi, L., et al. 2014, *MNRAS*, 443, 624, doi: 10.1093/mnras/stu1177
- Esteban, C., Peimbert, M., Torres-Peimbert, S., & Rodríguez, M. 2002, *ApJ*, 581, 241, doi: 10.1086/344104
- Fabbian, D., Nissen, P. E., Asplund, M., Pettini, M., & Akerman, C. 2009, *A&A*, 500, 1143, doi: 10.1051/0004-6361/200810095
- Finlator, K., & Davé, R. 2008, *MNRAS*, 385, 2181, doi: 10.1111/j.1365-2966.2008.12991.x
- Frankel, N., Rix, H.-W., Ting, Y.-S., Ness, M., & Hogg, D. W. 2018, *ApJ*, 865, 96, doi: 10.3847/1538-4357/aadba5
- Frankel, N., Sanders, J., Ting, Y.-S., & Rix, H.-W. 2020, *ApJ*, 896, 15, doi: 10.3847/1538-4357/ab910c
- Frebel, A., & Norris, J. E. 2015, *ARA&A*, 53, 631, doi: 10.1146/annurev-astro-082214-122423
- Frinchaboy, P. M., Thompson, B., Jackson, K. M., et al. 2013, *ApJ*, 777, L1, doi: 10.1088/2041-8205/777/1/L1
- Gaia Collaboration, Prusti, T., de Bruijne, J. H. J., et al. 2016, *A&A*, 595, A1, doi: 10.1051/0004-6361/201629272
- García Pérez, A. E., Allende Prieto, C., Holtzman, J. A., et al. 2016, *AJ*, 151, 144, doi: 10.3847/0004-6256/151/6/144
- García-Rojas, J., & Esteban, C. 2007, *ApJ*, 670, 457, doi: 10.1086/521871
- Gilroy, K. K. 1989, *ApJ*, 347, 835, doi: 10.1086/168173
- Griffith, E., Johnson, J. A., & Weinberg, D. H. 2019, *ApJ*, 886, 84, doi: 10.3847/1538-4357/ab4b5d

- Griffith, E. J., Sukhbold, T., Weinberg, D. H., et al. 2021, *ApJ*, 921, 73, doi: 10.3847/1538-4357/ac1bac
- Harris, C. R., Millman, K. J., van der Walt, S. J., et al. 2020, *Nature*, 585, 357, doi: 10.1038/s41586-020-2649-2
- Hasselquist, S., Holtzman, J. A., Shetrone, M., et al. 2019, *ApJ*, 871, 181, doi: 10.3847/1538-4357/aaf859
- Hayden, M. R., Holtzman, J. A., Bovy, J., et al. 2014, *AJ*, 147, 116, doi: 10.1088/0004-6256/147/5/116
- Helmi, A., Babusiaux, C., Koppelman, H. H., et al. 2018, *Nature*, 563, 85, doi: 10.1038/s41586-018-0625-x
- Henry, R. B. C., Edmunds, M. G., & Köppen, J. 2000, *ApJ*, 541, 660, doi: 10.1086/309471
- Hirschi, R. 2007, *A&A*, 461, 571, doi: 10.1051/0004-6361:20065356
- Hunter, J. D. 2007, *Computing in Science & Engineering*, 9, 90, doi: 10.1109/MCSE.2007.55
- Iben, Icko, J. 1967, *ARA&A*, 5, 571, doi: 10.1146/annurev.aa.05.090167.003035
- Izotov, Y. I., Thuan, T. X., & Guseva, N. G. 2012, *A&A*, 546, A122, doi: 10.1051/0004-6361/201219733
- James, B. L., Koposov, S., Stark, D. P., et al. 2015, *MNRAS*, 448, 2687, doi: 10.1093/mnras/stv175
- Johnson, J. A. 2019, *Science*, 363, 474, doi: 10.1126/science.aau9540
- Johnson, J. W., & Weinberg, D. H. 2020, *MNRAS*, 498, 1364, doi: 10.1093/mnras/staa2431
- Johnson, J. W., Weinberg, D. H., Vincenzo, F., Bird, J. C., & Griffith, E. J. 2023, *MNRAS*, 520, 782, doi: 10.1093/mnras/stad057
- Johnson, J. W., Weinberg, D. H., Vincenzo, F., et al. 2021, *MNRAS*, 508, 4484, doi: 10.1093/mnras/stab2718

- Johnson, J. W., Conroy, C., Johnson, B. D., et al. 2022, arXiv e-prints, arXiv:2210.01816, doi: 10.48550/arXiv.2210.01816
- Karakas, A. I. 2010, MNRAS, 403, 1413, doi: 10.1111/j.1365-2966.2009.16198.x
- Karakas, A. I., & Lattanzio, J. C. 2014, PASA, 31, e030, doi: 10.1017/pasa.2014.21
- Karakas, A. I., & Lugaro, M. 2016, ApJ, 825, 26, doi: 10.3847/0004-637X/825/1/26
- Karakas, A. I., Lugaro, M., Carlos, M., et al. 2018, MNRAS, 477, 421, doi: 10.1093/mnras/sty625
- Kennicutt, Robert C., J. 1998, ARA&A, 36, 189, doi: 10.1146/annurev.astro.36.1.189
- Kollmeier, J. A., Zasowski, G., Rix, H.-W., et al. 2017, arXiv e-prints, arXiv:1711.03234, doi: 10.48550/arXiv.1711.03234
- Korn, A. J., Grundahl, F., Richard, O., et al. 2007, ApJ, 671, 402, doi: 10.1086/523098
- Kroupa, P. 2001, MNRAS, 322, 231, doi: 10.1046/j.1365-8711.2001.04022.x
- Laird, J. B. 1985, ApJ, 289, 556, doi: 10.1086/162916
- Lambert, D. L., Gustafsson, B., Eriksson, K., & Hinkle, K. H. 1986, ApJS, 62, 373, doi: 10.1086/191145
- Lambert, D. L., & Ries, L. M. 1981, ApJ, 248, 228, doi: 10.1086/159147
- Larson, R. B. 1972, Nature Physical Science, 236, 7, doi: 10.1038/physci236007a0
- . 1974, MNRAS, 166, 585, doi: 10.1093/mnras/166.3.585
- Licquia, T. C., & Newman, J. A. 2015, ApJ, 806, 96, doi: 10.1088/0004-637X/806/1/96
- Lilly, S. J., Carollo, C. M., Pipino, A., Renzini, A., & Peng, Y. 2013, ApJ, 772, 119, doi: 10.1088/0004-637X/772/2/119
- Limongi, M., & Chieffi, A. 2018, ApJS, 237, 13, doi: 10.3847/1538-4365/aac24

- Lind, K., Korn, A. J., Barklem, P. S., & Grundahl, F. 2008, *A&A*, 490, 777, doi: 10.1051/0004-6361:200810051
- Loebman, S. R., Ivezić, Ž., Quinn, T. R., et al. 2012, *ApJ*, 758, L23, doi: 10.1088/2041-8205/758/1/L23
- Majewski, S. R., Schiavon, R. P., Frinchaboy, P. M., et al. 2017, *AJ*, 154, 94, doi: 10.3847/1538-3881/aa784d
- Maoz, D., Mannucci, F., & Brandt, T. D. 2012, *MNRAS*, 426, 3282, doi: 10.1111/j.1365-2966.2012.21871.x
- Martig, M., Fouesneau, M., Rix, H.-W., et al. 2016, *MNRAS*, 456, 3655, doi: 10.1093/mnras/stv2830
- Masseron, T., & Gilmore, G. 2015, *MNRAS*, 453, 1855, doi: 10.1093/mnras/stv1731
- Matteucci, F. 2021, *A&A Rev.*, 29, 5, doi: 10.1007/s00159-021-00133-8
- Minchev, I., Chiappini, C., & Martig, M. 2013, *A&A*, 558, A9, doi: 10.1051/0004-6361/201220189
- . 2014, *A&A*, 572, A92, doi: 10.1051/0004-6361/201423487
- Morrison, S., Kulkarni, V. P., Som, D., et al. 2016, *ApJ*, 830, 158, doi: 10.3847/0004-637X/830/2/158
- Nissen, P. E., Chen, Y. Q., Carigi, L., Schuster, W. J., & Zhao, G. 2014, *A&A*, 568, A25, doi: 10.1051/0004-6361/201424184
- Nomoto, K., Kobayashi, C., & Tominaga, N. 2013, *ARA&A*, 51, 457, doi: 10.1146/annurev-astro-082812-140956
- Ohio Supercomputer Center. 1987, Ohio Supercomputer Center. <http://osc.edu/ark:/19495/f5s1ph73>
- Pagel, B. E. J. 2009, *Nucleosynthesis and Chemical Evolution of Galaxies*, 2nd edn. (Cambridge University Press), doi: 10.1017/CBO9780511812170
- pandas development team, T. 2020, pandas-dev/pandas: Pandas, latest, Zenodo, doi: 10.5281/zenodo.3509134

- Peeples, M. S., & Shankar, F. 2011, MNRAS, 417, 2962, doi: 10.1111/j.1365-2966.2011.19456.x
- Pérez, F., & Granger, B. E. 2007, Computing in Science and Engineering, 9, 21, doi: 10.1109/MCSE.2007.53
- Pettini, M., Zych, B. J., Steidel, C. C., & Chaffee, F. H. 2008, MNRAS, 385, 2011, doi: 10.1111/j.1365-2966.2008.12951.x
- Pilyugin, L. S., Vílchez, J. M., & Thuan, T. X. 2010, ApJ, 720, 1738, doi: 10.1088/0004-637X/720/2/1738
- Sánchez, S. F. 2020, ARA&A, 58, 99, doi: 10.1146/annurev-astro-012120-013326
- Sellwood, J. A., & Binney, J. J. 2002, MNRAS, 336, 785, doi: 10.1046/j.1365-8711.2002.05806.x
- Skillman, E. D., Berg, D. A., Pogge, R. W., et al. 2020, ApJ, 894, 138, doi: 10.3847/1538-4357/ab86ae
- Souto, D., Cunha, K., Smith, V. V., et al. 2018, ApJ, 857, 14, doi: 10.3847/1538-4357/aab612
- Souto, D., Allende Prieto, C., Cunha, K., et al. 2019, ApJ, 874, 97, doi: 10.3847/1538-4357/ab0b43
- Spitoni, E., Silva Aguirre, V., Matteucci, F., Calura, F., & Grisoni, V. 2019, A&A, 623, A60, doi: 10.1051/0004-6361/201834188
- Spitoni, E., Verma, K., Silva Aguirre, V., & Calura, F. 2020, A&A, 635, A58, doi: 10.1051/0004-6361/201937275
- Spitoni, E., Verma, K., Silva Aguirre, V., et al. 2021, A&A, 647, A73, doi: 10.1051/0004-6361/202039864
- Srianand, R., Gupta, N., Petitjean, P., Noterdaeme, P., & Ledoux, C. 2010, MNRAS, 405, 1888, doi: 10.1111/j.1365-2966.2010.16574.x
- Sukhbold, T., Ertl, T., Woosley, S. E., Brown, J. M., & Janka, H. T. 2016, ApJ, 821, 38, doi: 10.3847/0004-637X/821/1/38
- Tacconi, L. J., Genzel, R., Saintonge, A., et al. 2018, ApJ, 853, 179, doi: 10.3847/1538-4357/aaa4b4

- Tinsley, B. M. 1980, *Fund. Cosmic Phys.*, 5, 287, doi: 10.48550/arXiv.2203.02041
- Ventura, P., Dell’Agli, F., Lugaro, M., et al. 2020, *A&A*, 641, A103, doi: 10.1051/0004-6361/202038289
- Ventura, P., Dell’Agli, F., Schneider, R., et al. 2014, *MNRAS*, 439, 977, doi: 10.1093/mnras/stu028
- Ventura, P., Di Criscienzo, M., Carini, R., & D’Antona, F. 2013, *MNRAS*, 431, 3642, doi: 10.1093/mnras/stt444
- Ventura, P., Karakas, A., Dell’Agli, F., García-Hernández, D. A., & Guzman-Ramirez, L. 2018, *MNRAS*, 475, 2282, doi: 10.1093/mnras/stx3338
- Vincenzo, F., Weinberg, D. H., Montalbán, J., et al. 2021, arXiv e-prints, arXiv:2106.03912. <https://arxiv.org/abs/2106.03912>
- Virtanen, P., Gommers, R., Oliphant, T. E., et al. 2020, *Nature Methods*, 17, 261, doi: 10.1038/s41592-019-0686-2
- Weinberg, D. H., Andrews, B. H., & Freudenburg, J. 2017, *ApJ*, 837, 183, doi: 10.3847/1538-4357/837/2/183
- Weinberg, D. H., Holtzman, J. A., Hasselquist, S., et al. 2019, *ApJ*, 874, 102, doi: 10.3847/1538-4357/ab07c7
- Weinberg, D. H., Holtzman, J. A., Johnson, J. A., et al. 2022, *ApJS*, 260, 32, doi: 10.3847/1538-4365/ac6028
- Woosley, S. E., & Weaver, T. A. 1995, *ApJS*, 101, 181, doi: 10.1086/192237
- Zolotov, A., Brooks, A. M., Willman, B., et al. 2012, *ApJ*, 761, 71, doi: 10.1088/0004-637X/761/1/71

Appendix

A.1 The APOGEE Subgiant Sample

I use the criteria outlined in Roberts et al. (2023, in prep.) to create a sample of subgiants from APOGEE DR17 Majewski et al. (2017) as our primary observational constraint. APOGEE is part of the Sloan Digital Sky Survey 17 and measures high resolution spectra of thousands of stars Abdurro’uf et al. (2022). Subgiants are reflective of birth abundances for CNO (Souto et al. 2019). with chemical abundance determinations from the APOGEE Stellar Parameter and Chemical Abundance Pipeline (ASPCAP) (García Pérez et al. 2016). Roberts et al. (2023, in prep.) select a region of stars in $\log g$ - T_{eff} space described by the following polyhedron

$$\begin{cases} \log g \geq 3.5 \\ \log g \leq 0.004T_{\text{eff}} - 15.7 \\ \log g \leq 0.000706T_{\text{eff}} + 0.36 \\ \log g \leq -0.0015T_{\text{eff}} + 12.05 \\ \log g \geq 0.0012T_{\text{eff}} - 2.8 \end{cases} \quad (\text{A1})$$

This cut isolates a clean sample of $\sim 12,000$ subgiants. As first dredge up, which affects C and N abundances, only occurs during the ascent onto the red giant branch, subgiant stars are unaffected by this enrichment.

Additionally, I included stars in APOGEE marked by the following flags.

- APOGEE_MIRCLUSTER_STAR
- APOGEE_EMISSION_STAR
- APOGEE_EMBEDDEDCLUSTER_STAR
- young cluster (IN-SYNC)
- APOGEE2_W345

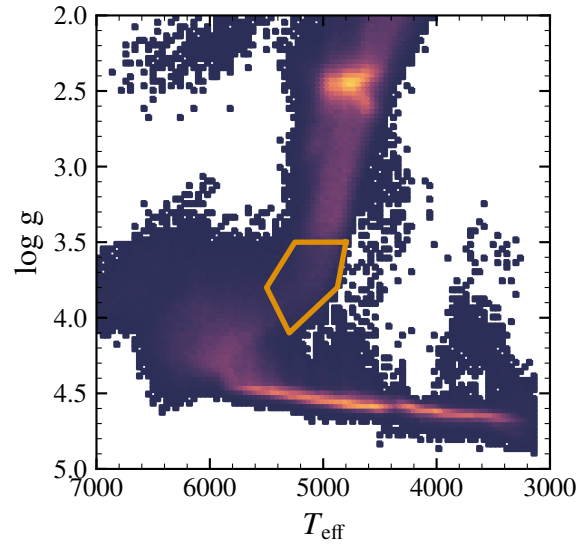


Figure A1: A Kiel diagram of APOGEE stars. Following Roberts et al. (2023, in prep.), we select subgiants in the orange polygon (see Equation A1). These stars have not yet experienced first dredge-up, so their photospheric C and N abundances should reflect their birth mixture.

- EB planet

A second approach in determining birth abundances in stars is to correct the surface abundance effects of first dredge up, as in Vincenzo et al. (2021). I note that there is a slight difference in the yields found through Vincenzo et al. (2021) and Roberts et al. (2023, in prep.). As o

$$\begin{cases} [\text{Mg}/\text{Fe}] > 0.12 - 0.13[\text{Fe}/\text{H}], & [\text{Fe}/\text{H}] < 0 \\ [\text{Mg}/\text{Fe}] > 0.12, & [\text{Fe}/\text{H}] > 0 \end{cases} \quad (\text{A2})$$

, discussion of GALAH C in Griffith et al. 2019).

I choose to use Roberts et al. (2023, in prep.)’s sample as this does not rely on additional layers of modeling, providing a more direct constraint to our model and limiting our systematic uncertainties.

A.2 Additional Considerations of Yields

As I focus on constraining relative yields, I neglect O and Mg yield variations in the main text. There is substantial variation in Mg predictions (see Fig. A3). Most models predict relatively flat Mg trends with metallicity (even with rotating models from Limongi & Chieffi 2018). However, the variation is significant and my adopted $y_{\text{Mg}}^{\text{CC}}$ yield is much higher than most models. This is a known problem (see Griffith et al. (2021)). ccsne models overpredict O or underpredict Mg, and the resolution is still unknown. My results are, however, independent of whether the ccsne element is O or Mg.

While I focus the main discussion of the paper on the C11 model, other AGB models can impact abundance trends when f_{AGB} becomes larger. Here, I briefly explore the effects of variations in AGB models that affect abundance trend predictions when these models are amplified to match observational $[\text{C}/\text{Mg}]$ - $[\text{Mg}/\text{Fe}]$ trends. See Fig A2.

V13 is also interesting as at high metallicity, the yields quickly become strongly negative. This causes a reversal of the $[\text{C}/\text{Mg}]$ - $[\text{Mg}/\text{Fe}]$ trend at high $[\text{Mg}/\text{H}]$ slices (figure ...). As our set of observations does not appear to reverse, this indicates that C yields are likely to stay positive even at slightly super-solar, so models like V13 are a poor match to observations.

In Fig. A4.

I leave the exploration of the age-metallicity relation for C to future work.

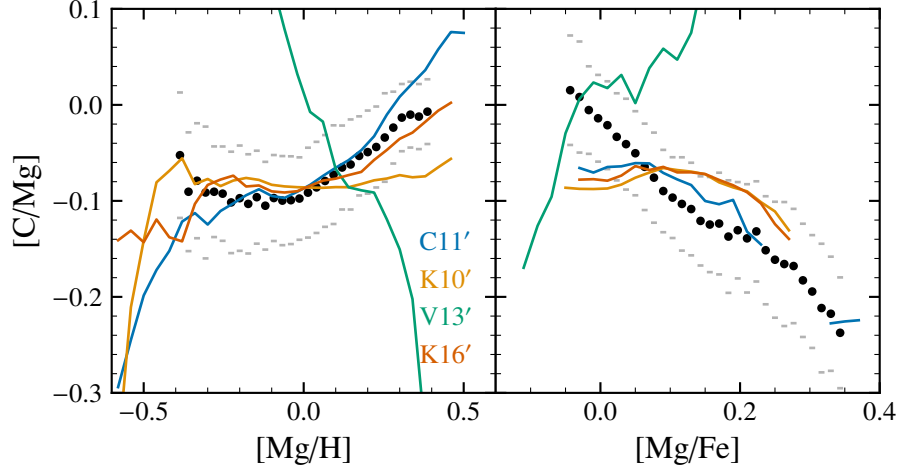


Figure A2: Same as Fig. 9 except where $f_{\text{agb}} = 0.2$. When yields are amplified, chaos ensues.

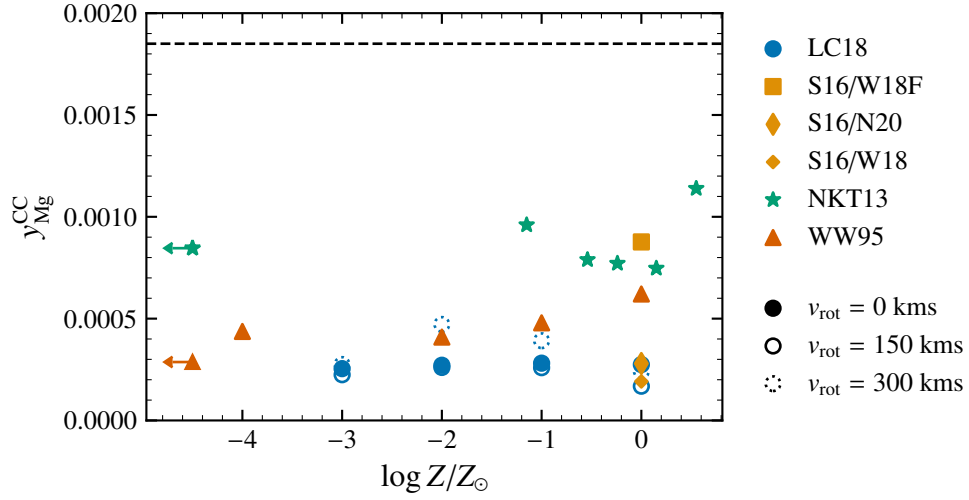


Figure A3: Same as the top panel of Fig. 6, but for Mg. Our Mg yield choice is shown as a dashed line at the top

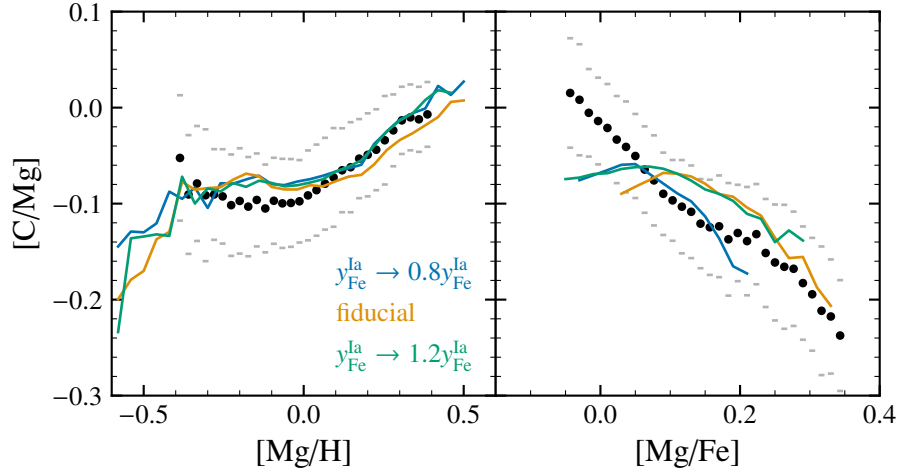


Figure A4: Similar to Fig. 9 except with variations of the SNE Ia iron fraction

A.3 Software

Software that has contributed to this work:

- Ohio Supercomputer Center (1987)
- VICE (Johnson & Weinberg 2020; Johnson et al. 2021)
- matplotlib (Hunter 2007)
- scipy (Virtanen et al. 2020)
- IPython (Pérez & Granger 2007)
- pandas (pandas development team 2020)
- numpy (Harris et al. 2020)
- astropy (Astropy Collaboration et al. 2013, 2018, 2022)
- seaborn

Symbols

| | |
|-------------------------------------|--|
| $[A/B]$ | The abundance ratio between elements A and B . See . |
| α_{CC} | The mass outflow loading factor. |
| α_{CC} | The mass outflow loading factor. |
| η | The mass outflow loading factor. |
| ζ | The massive star carbon yield metallicity dependence. |
| $\dot{\Sigma}$ | The massive star carbon yield metallicity dependence. |
| M_{\odot} | The mass of the sun. $M_{\odot} = 1.989 \times 10^{33}$ g. |
| \dot{M}_{\star} | The rate of star formation. |
| f_{AGB} | The fractional contribution of AGB stars to the total IMF-averaged carbon yield at solar metallicity.. |
| $\tilde{y}_{\text{C}}^{\text{AGB}}$ | The net fraction initial-mass-function weighted low-mass star yield of carbon. |
| $y_{\text{C}}^{\text{AGB}}$ | The net fraction initial-mass-function weighted low-mass star yield of carbon. |
| y_{C}^{CC} | The net fraction initial-mass-function weighted massive star yield of carbon. |
| $y_{\text{Mg}}^{\text{CC}}$ | The net fraction initial-mass-function weighted massive star yield of magnesium. |
| Z_{\odot} | The metallicity for the sun. |
| Z | The metallicity fraction. |

Stellar Yield Models

- C11** the yield set from Cristallo et al. (2011, 2015). The models were run at $M = 1.3, 1.5, 2.0, 2.5, 3.0, 4.0, 5.0, 6.0$ and $Z = 0.0001, 0.0003, 0.001, 0.002, 0.003, 0.006, 0.008, 0.01, 0.014, 0.02..$
- K10** the yield set from Karakas (2010). Includes models run at $M = 1.0, 1.25, 1.5, 1.75, 1.9, 2.25, 2.5, 3.0, 3.5, 4.0, 4.5, 5.0, 5.5, 6.0$ and $Z = 0.0001, 0.004, 0.008, 0.02.$
- K16** The yield set from Karakas & Lugaro (2016); Karakas et al. (2018). The model is sampled at $M = (0.0003, 0.001, 0.002, 0.004, 0.008, 0.014, 0.04)$ and $Z = (0.0003, 0.001, 0.002, 0.004, 0.008, 0.014, 0.04).$
- V13** the $_{\text{AGB}}$ yield set from Ventura et al. (2013, 2014, 2018, 2020). Includes models with masses $m = (1.5, 2.0, 2.5, 3.0, 3.5, 4.0, 4.5, 5.0, 6.0, 6.5, 7.0)$ and with metallicities $Z = (0.0003, 0.001, 0.002, 0.004, 0.008, 0.014, 0.04).$

Acronyms

AGB Dying low-mass stars. Produces C, N, and heavy s-process elements..

APOGEE Apache Point Observatory Galactic Evolution Experiment.

CCSNE Core collapse supernovae. Massive star explosions. CCSNE produce many elements including α -elements, Fe-peak elements, and r and s-process elements..

DLA Damped Lyman-alpha system. DLAs are clouds of gas from the early universe which are observed through their absorption of quasar spectra. The name comes from the strong Lyman-alpha lines (1216 Å) due to H absorption..

GCE galactic chemical evolution.

IMF initial mass function.

SFH star formation history.

SNE IA Exploding white dwarfs, produces Fe-peak elements.

SSP single stellar population.

Glossary

- IMF-averaged** Initial-mass function 2.0, 2.1, 3.0, A.3
- hot bottom burning** Third dredge up occurs when 2.1
- metallicity** the (mass) fraction of a star or gas which is not made of either hydrogen or helium. For the sun, the metallicity is $Z_{\odot} = 0.014$. 1.0, 2.1
- multi-zone** the synthesis of new elements inside stars. 4.0, 6.0
- nucleosynthesis** the synthesis of new elements inside stars. 2.0, 6.0
- one-zone** the synthesis of new elements inside stars. 3.0, 4.0
- red giant branch** Red giant branch stars are stars which have completed hydrogen core burning and have expanded in size.. 1.0, 5.1, A.1
- subgiant** A subgiant is.... 1.0, 3.1, 5.1, 5.6, 5.7, 6.0, A.1
- third dredge up** Third dredge up occurs when 2.1
- yield** the synthesis of new elements inside stars. 1.0, 2.0